Article

Developmental Cell

# Aged intestinal stem cells propagate cell-intrinsic sources of inflammaging in mice

## Graphical abstract

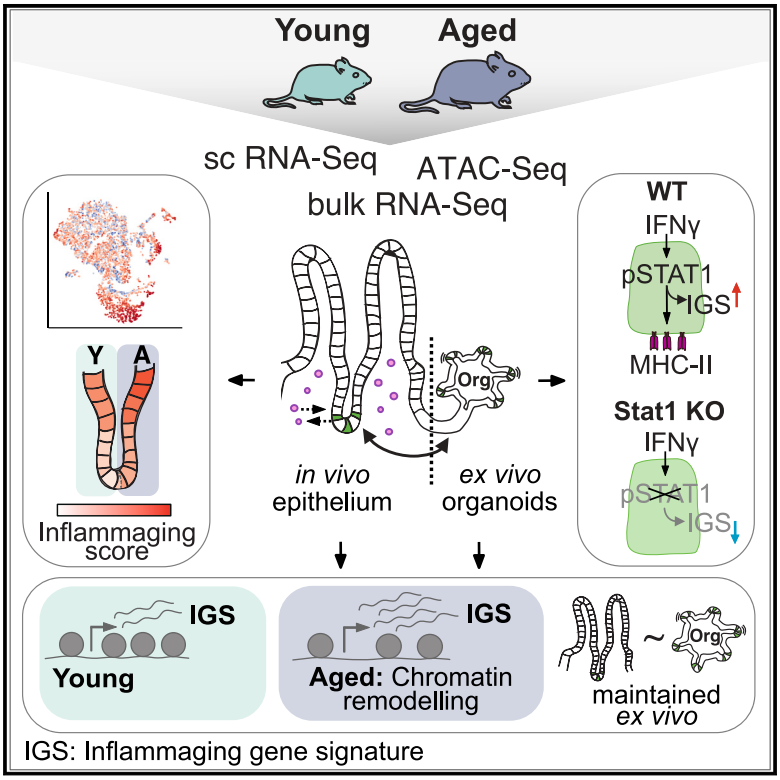


## Highlights

- Inflammaging establishes differently along the intestinal crypt-villus axis
- Aged ISCs upregulate MHC-II for CD4$^+$ T cell interaction via IFNγ-STAT1 signaling
- *In vivo*-acquired changes in chromatin accessibility are maintained in organoids
- Aged ISCs propagate cell-intrinsic sources of inflammaging to the epithelium

## Authors

Maja C. Funk, Jan G. Gleixner, Florian Heigwer, ..., Simon Haas, Mathias Heikenwalder, Michael Boutros

## Correspondence

m.boutros@dkfz.de

## In brief

Funk et al. identify at the single-cell level that intestinal inflammaging in mice develops differently along the crypt-villus axis. Moreover, epithelial cells acquire *in vivo* age-specific changes in chromatin accessibility that are maintained *ex vivo* in organoid cultures and associated with inflammation-associated loci, promoting stem cell-intrinsic sources of inflammaging.

Funk et al., 2023, Developmental Cell *58*, 2914–2929
December 18, 2023 
https://doi.org/10.1016/j.devcel.2023.11.013

CellPress

CellPress
OPEN ACCESS

Developmental Cell

Article

# Aged intestinal stem cells propagate cell-intrinsic sources of inflammaging in mice

Maja C. Funk,[1] Jan G. Gleixner,[1,2,3,4] Florian Heigwer,[1,5] Dominik Vonficht,[4,6,7] Erica Valentini,[1] Zeynep Aydin,[1] Elena Tonin,[1] Stefania Del Prete,[8] Sylvia Mahara,[9] Yannick Throm,[1] Jenny Hetzer,[10] Danijela Heide,[10] Oliver Stegle,[2,3] Duncan T. Odom,[8] Angelika Feldmann,[9] Simon Haas,[6,7,11,12] Mathias Heikenwalder,[10,13] and Michael Boutros[1,14,*]

[1]German Cancer Research Center (DKFZ), Division Signaling and Functional Genomics, Heidelberg University, BioQuant & Department of Cell and Molecular Biology, Medical Faculty Mannheim, Heidelberg University, Institute for Human Genetics, Medical Faculty Heidelberg, 69120 Heidelberg, Germany
[2]German Cancer Research Center (DKFZ), Division of Computational Genomics and Systems Genetics, 69120 Heidelberg, Germany
[3]Genome Biology Unit, European Molecular Biology Laboratory (EMBL), 69117 Heidelberg, Germany
[4]Faculty of Biosciences, Heidelberg University, 69117 Heidelberg, Germany
[5]Department of Life Sciences and Engineering, University of Applied Sciences Bingen, 55411 Bingen am Rhein, Germany
[6]Heidelberg Institute for Stem Cell Technology and Experimental Medicine, (HI-STEM gGmbH), 69120 Heidelberg, Germany
[7]German Cancer Research Center (DKFZ), Division of Stem Cells and Cancer, DKFZ-ZMBH Alliance, 69120 Heidelberg, Germany
[8]German Cancer Research Center (DKFZ), Division Regulatory Genomics and Cancer Evolution, 69120 Heidelberg, Germany
[9]German Cancer Research Center (DKFZ), Junior Research Group Mechanisms of Genome Control, 69120 Heidelberg, Germany
[10]German Cancer Research Center (DKFZ), Division Chronic Inflammation and Cancer, 69120 Heidelberg, Germany
[11]Berlin Institute of Health (BIH), Charité – Universitätsmedizin Berlin, 10178 Berlin, Germany
[12]Max Delbrück Center for Molecular Medicine in the Helmholtz Association, Berlin Institute for Medical Systems Biology, 10115 Berlin, Germany
[13]M3 Research Center, Medical Faculty Tübingen, Eberhard Karls University of Tübingen, 72074 Tübingen, Germany
[14]Lead contact
*Correspondence: m.boutros@dkfz.de
https://doi.org/10.1016/j.devcel.2023.11.013

## SUMMARY

Low-grade chronic inflammation is a hallmark of ageing, associated with impaired tissue function and disease development. However, how cell-intrinsic and -extrinsic factors collectively establish this phenotype, termed inflammaging, remains poorly understood. We addressed this question in the mouse intestinal epithelium, using mouse organoid cultures to dissect stem cell-intrinsic and -extrinsic sources of inflammaging. At the single-cell level, we found that inflammaging is established differently along the crypt-villus axis, with aged intestinal stem cells (ISCs) strongly upregulating major histocompatibility complex class II (MHC-II) genes. Importantly, the inflammaging phenotype was stably propagated by aged ISCs in organoid cultures and associated with increased chromatin accessibility at inflammation-associated loci *in vivo* and *ex vivo*, indicating cell-intrinsic inflammatory memory. Mechanistically, we show that the expression of inflammatory genes is dependent on STAT1 signaling. Together, our data identify that intestinal inflammaging in mice is promoted by a cell-intrinsic mechanism, stably propagated by ISCs, and associated with a disbalance in immune homeostasis.

## INTRODUCTION

During ageing, cell-intrinsic and -extrinsic factors act in concert, leading to impaired tissue function and onset of age-related diseases.[1,2] An organ that is particularly exposed to external signals is the intestine. During homeostasis, the intestine forms a dynamic interface with the microenvironment and serves as a protective barrier against external stimuli.[3–5] Furthermore, the intestinal epithelium mediates the host's immune response to clear invading pathogens and to provide tolerance against the commensal microbiome.[5]

To maintain tissue homeostasis, the small intestine relies on highly proliferative stem cells to continuously renew the entire epithelium. Intestinal stem cells (ISCs) reside in their protective stem cell niche called crypt. New progenitor cells leave the crypt, enter the transit-amplifying zone, and are pushed upward toward the villi, the functional units of the intestine.[6] Along the crypt-villus axis, different cell types can be found: ISCs, absorptive enterocytes as well as secretory cells, including Paneth cells (PCs), goblet cells (GCs), enteroendocrine cells (EECs), and chemosensory Tuft cells.[7] PCs, intercalated between the ISCs, are part of the stem cell niche and secrete growth factors essential for proper stem cell function and antimicrobial peptides as a first-line defense against invading microbes.[8] Additionally, immune cells and the microbiome in the intestinal microenvironment can directly regulate ISC function and epithelial homeostasis.[9–11]

 

Upon ageing, ISC regeneration capacity is impaired,[12–14] in part due to reduced canonical Wnt signaling in ISCs, neighboring PCs, and the subepithelial mesenchyme.[13,14] Moreover, the ISC niche and entire epithelium are exposed to extrinsic factors from the microenvironment, which by themselves are subject to age-related changes.[4] During ageing, direct interaction with immune cells and the microbiome causes chronic inflammation in the intestine,[15–17] an ageing phenotype known as inflammaging.[18,19] However, it remains poorly understood how extrinsic factors act in concert with ISC-intrinsic changes to establish and maintain chronic inflammation during ageing.

To identify cell-intrinsic and -extrinsic sources of increased inflammatory signaling as well as to unveil how they interact and reinforce each other, we first assessed age-related transcriptional changes in the freshly isolated in vivo intestinal epithelium. At the single-cell level, we show that inflammaging develops differently in cells along the crypt-villus axis and is marked by the upregulation of major histocompatibility complex class II (MHC-II) antigen presentation machinery in ISCs. Elevated MHC-II levels on aged ISCs are associated with compositional changes in the T cell compartment and an increase in physical interaction between aged ISCs and $CD4^+$ T cells. To dissect whether the observed inflammaging phenotype is driven by cell-intrinsic or -extrinsic sources, we used intestinal organoids, which were cultured *ex vivo*, shielded from extrinsic signals, and constantly renewed from a limited stem cell population. These experiments demonstrated that cell-intrinsic inflammaging signatures persist in culture, independent of external signals from the microenvironment, and are stably propagated by ISCs over time. Analysis of open chromatin accessibility in organoids and freshly isolated epithelial cells further identified that the ISC-intrinsic inflammaging is primed at the chromatin level, established *in vivo*, and maintained in culture, suggesting the development of a memory of inflammation. Mechanistically, our data show that the expression of inflammaging signature genes is dependent on signal transducer and activator of transcription 1 (STAT1) signaling.

In summary, we identify the establishment of a cell-intrinsic inflammaging phenotype that is stably propagated by ISCs and associated with chromatin remodeling of inflammation-associated loci. These findings provide insights into how chronic inflammatory states evolve over time and how ISCs might contribute to systemic inflammation and the disbalance of immune homeostasis during ageing.

## RESULTS

### Intestinal epithelial cells develop chronic inflammation during ageing

To first investigate the *in vivo* ageing effect in all epithelial cell types of the intestine, we performed bulk and single-cell RNA sequencing (scRNA-seq) from freshly isolated epithelial cells ($EpCam^+$, $CD45^-$) from the proximal small intestine of three young and aged mice each (Figure 1A). In a principal-component analysis (PCA) of the bulk RNA-seq samples, the age of the mice was the major source of variance, suggesting drastic age-related transcriptomic changes (Figure S1A). Indeed, we identified 508 genes significantly differentially expressed upon ageing, of which 190 genes were upregulated and 318 genes were downregulated (Figures 1B and S1B). Downregulated genes included alpha-defensins (*Defa3*, *Defa17*, *Defa24*, and *Defa26*) (Figures 1B and S1C), which are specifically secreted by PCs for antimicrobial defense,[20] indicating a diminished functionality of PCs and mucosal immunity upon ageing. We also detected reduced Wnt3 in the aged epithelium (Figure 1B), consistent with previous reports of decreased Wnt signaling during intestinal ageing.[13,14] Upregulated genes comprised various immune response and interferon-inducible genes, such as *Igtp*, *Ly6e*, *Ccr2*, *Ifitm3*, *P2rx7*, and *Ifi47* (Figures 1B and 1C). To gain functional insights into the ageing phenotype of the intestine, we performed a gene set enrichment analysis (GSEA) (Figure 1D). This analysis identified an enrichment for ageing-associated processes, including mechanistic target of rapamycin complex 1 (mTORC1) signaling, which has been previously linked to intestinal ageing.[14,21] The most prominent alteration was an enrichment of inflammation-associated signaling pathways, including interferon-gamma (IFN-γ) and -alpha (IFN-α) response signatures as well as allograft rejection, tumor necrosis factor alpha (TNF-α) signaling via nuclear factor κB (NF-κB), inflammatory response, and IL6-JAK-STAT3 signaling. Low-grade chronic inflammation during ageing is known as inflammaging,[18,19] and we collectively defined the genes of these six inflammation-associated gene sets as *Inflammaging gene set*, which comprises in total 689 genes (Table S1). Accordingly, we also found increased expression of genes encoding for interferon-inducible guanylate-binding proteins (Gbps) (*Gbp2*, *6*, *7*, *8*, *9*) (Figure S1D), which are involved in inflammasome activation.[22] Most notably, we identified several genes involved in major histocompatibility class II complex (MHC-II)-mediated antigen presentation highly upregulated in the aged intestinal epithelium, including the invariant chain *Cd74* and the MHC-II transactivator *Ciita* (Figures 1B and 1C). Immunohistochemistry (IHC) staining confirmed a striking upregulation of MHC-II on the protein level in the epithelium of aged mice, including intestinal crypts, where ISCs are located (Figures 1E–1G).

In summary, our bulk RNA-seq approach identified that the aged intestinal epithelium shows signs of reduced mucosal immunity and develops a pronounced inflammaging phenotype in intestinal epithelial cells (IECs), including ISCs.

### Inflammaging establishes differently in cells along the crypt-villus axis

Next, we aimed to identify individual ageing phenotypes for all epithelial cell types and to assess how the different cell types are affected by inflammaging. To this end, we isolated and sequenced single epithelial cells ($EpCam^+$, $CD45^-$) from the small intestine of three young and aged mice (Figure 1A). Transcriptomes with more than 10,000 total counts and less than 15% of counts from mitochondrial genes passed our quality control, resulting in 13,360 high-quality transcriptomes (8,240 from young and 5,140 from aged mice) (Figures S2A–S2C). To assign a cell type to each of our single-cell transcriptomes, we transferred refined cell-type labels from a reference dataset[23] for each replicate independently. This approach enabled us to distinguish all known intestinal cell types (Figures 2A and S2D) at similar fractions as reported previously[23] (Figure S1E). Importantly, all identified cell-type clusters corresponded to epithelial cell types, strongly indicating that our results were not

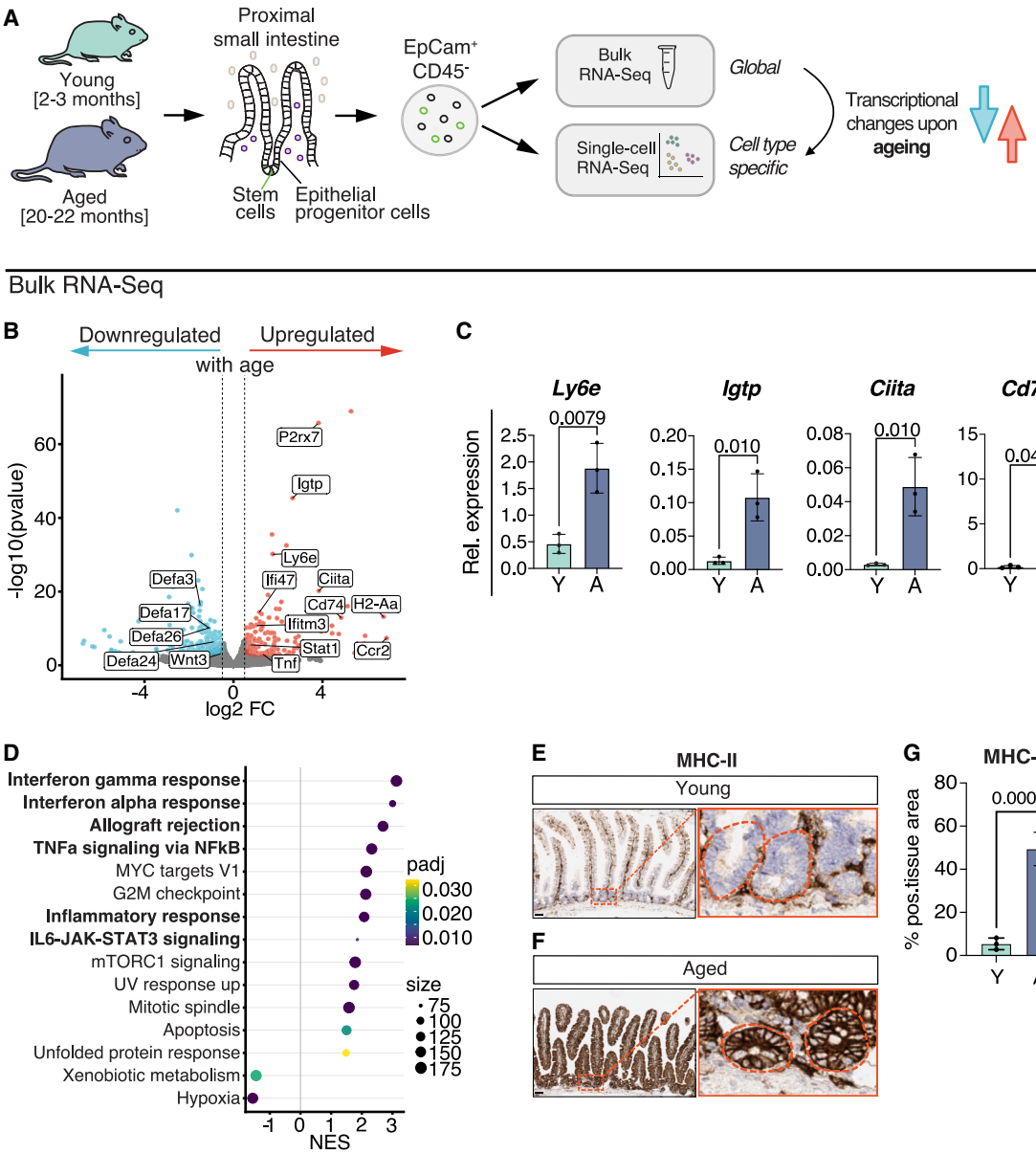


**Figure 1. Intestinal epithelial cells develop chronic inflammation during ageing**

(A) Schematic of the experimental approach of bulk and single-cell RNA-seq.

(B) Volcano plot showing differentially expressed genes upon ageing (aged over young) in the small intestinal epithelium; red, significantly (false discovery rate, FDR $\leq$ 10%) upregulated ($\log_2$ fold change, FC > 0.5); blue, significantly downregulated ($\log_2$ FC < [−0.5]); gray, not significant and absolute $\log_2$ FC < 0.5.

(C) Transcriptional changes of *Ly6e, Igtp*, *Cd74*, and *Ciita* upon ageing in the small intestinal epithelium. Normalized transcript levels were assessed by quantitative real-time PCR. Data are represented as mean ± SD, and data points represent biological replicates. Statistical significance was tested by an unpaired t test (two-sided).

(D) Normalized enrichment score (NES) based on gene set enrichment analysis upon ageing on hallmark gene sets (MSigDB), filtered for (FDR $\leq$ 5%).

(E and F) IHC staining for MHC-II on whole intestinal tissue sections from young (E) and aged (F) mice. Inlet highlights intestinal crypt regions; scale bars, 50 μm.

(G) MHC-II staining in (E) and (F) quantified as positive tissue area (n = 3 per young and aged mice). Data are represented as mean ± SD.

See also Figure S1 and Table S1.

confounded by the presence of non-epithelial cells, such as hematopoietic cells. In a t-distributed stochastic neighbor embedding (tSNE), young and aged cells were evenly distributed across the different clusters, and the quantification of the fraction of cells per cell type did not detect substantial differences upon ageing (Figures 2B and S1H–S1J). PCA for all cell types together showed that cell-type identity was largely maintained during ageing (Figure S1F), while within individual cell types, the age of the mice displayed the major source of variance between the samples (Figure S1G). These results identified robust transcriptomic changes in the aged epithelium at single-cell and cell-type levels.

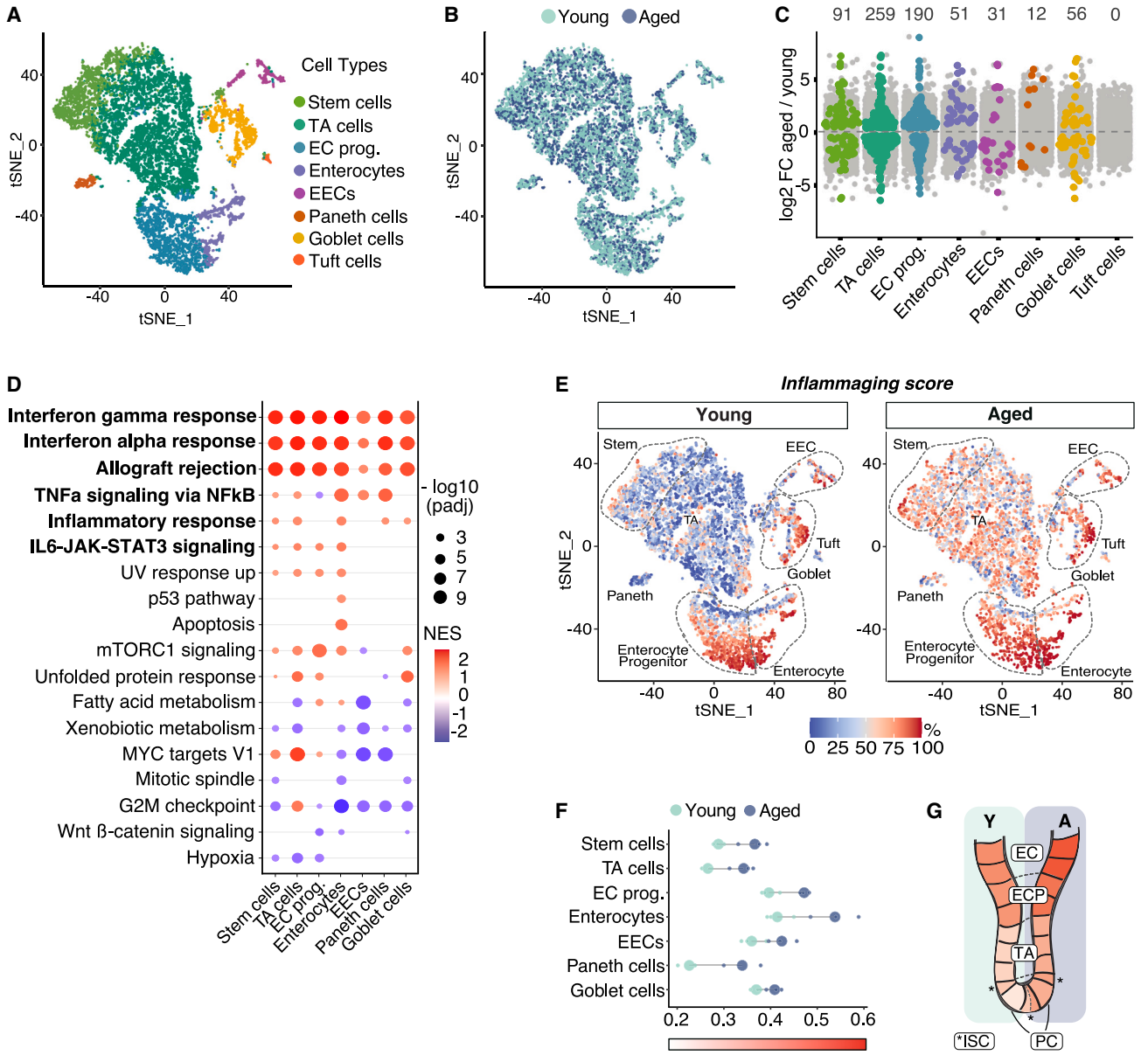


**Figure 2. Inflammaging establishes differently in cells along the crypt-villus axis**

(A) Cell-type assignment of all 13,360 sequenced cells from six different mice (3 young and 3 aged mice) visualized in a tSNE embedding.

(B) tSNE visualization of all 13,360 sequenced cells, color-coded by the age of the respective mouse.

(C) Number of differentially expressed genes in the small intestinal epithelium in young and aged mice per cell type. Significantly (FDR $\leq$ 10%) differentially expressed genes are colored in the respective cell-type-specific color; not significantly changed genes are displayed in gray.

(D) Gene set enrichment analysis identifies broad enrichment of inflammaging gene sets in all cell types. Normalized enrichment score (NES) based on gene set enrichment analysis on hallmark gene sets for all cell types, filtered for FDR of $\leq$5%.

(E) tSNE visualization of all young and aged cells separate and color-coded for their individual inflammaging score (quantile normalized).

(F) Inflammaging score calculated for each cell type and for each sample (3 young and 3 aged mice).

(G) Schematic of intestinal crypt (ISCs, PCs, and TA cells), enterocyte progenitors (ECP), and enterocytes (EC). Left side shows young intestine, while right side shows aged intestine. Color indicates the level of inflammaging according to the color scale in (F).

$Log_2$ FC, $log_2$ fold change; TA, transit-amplifying cells; EC prog, enterocyte progenitors; EECs, enteroendocrine cells.

See also Figures S1 and S2.

To determine transcriptional changes upon ageing in ISCs and IECs individually, we examined differentially expressed genes (DEGs) for each cell type (Figure 2C). We identified significant DEGs in all cell types, except in Tuft cells, due to the low number of sequenced cells leading to insufficient statistical power. With 259 genes, we detected the highest number of DEGs in transit-amplifying cells (TA cells), while in ISCs, 91 genes were significantly changed upon ageing. Functionally, we

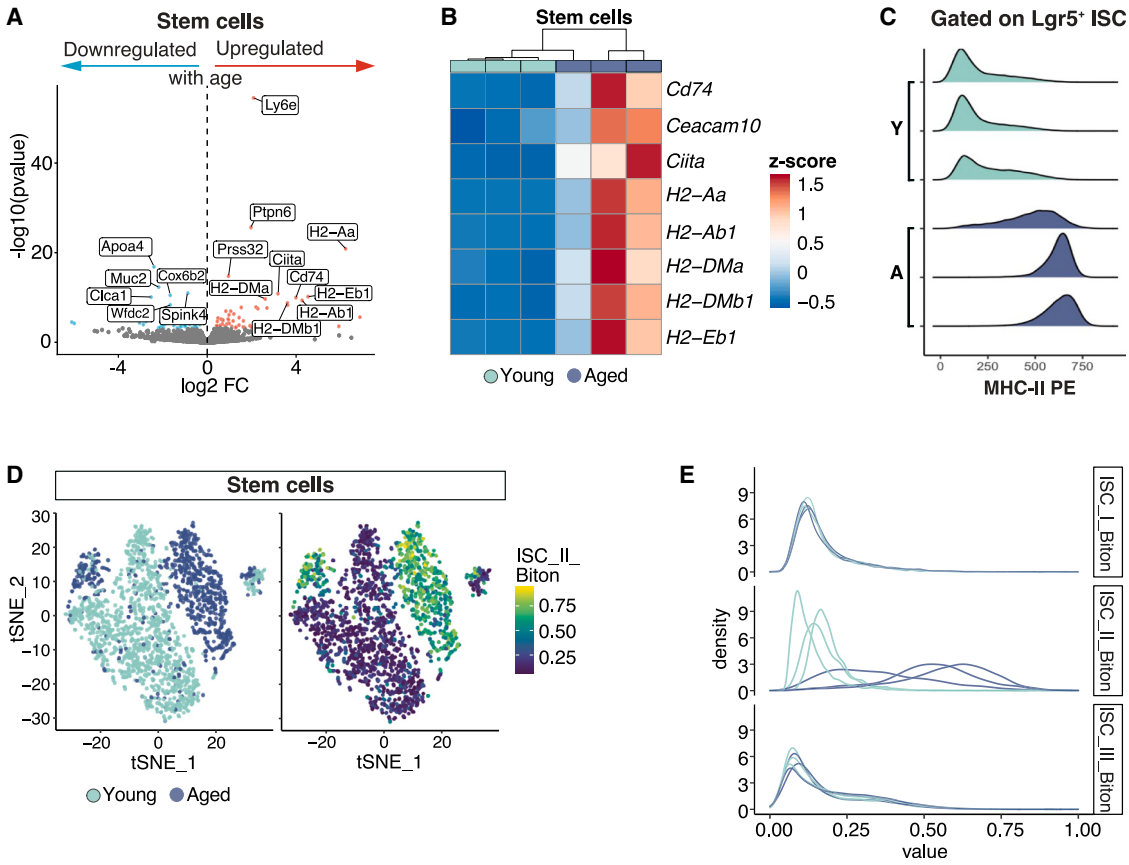


**Figure 3. MHC-II upregulation as a hallmark of inflammaging in aged ISCs**

(A) Volcano plot showing differentially expressed genes (DEGs) upon ageing in ISCs; red, significantly (FDR ≤ 10%) upregulated; blue, significantly downregulated; gray, not significant. The 20 most significant DEGs are labeled.

(B) Upregulation of MHC-II gene expression in aged ISCs. Relative mean expression as *Z* score per MHC-II gene (row) and sample (column).

(C) Histograms depicting MHC-II surface expression in young and aged Lgr5$^+$ ISCs, measured by flow cytometry.

(D) tSNE embedding of ISCs only, colored by age and by rescaled similarity to ISC-II cells of Biton et al.[10] (Biton-ISC-II score): ISC age is major source of variation and correlated with ISC-II-score.

(E) Distribution of Biton-ISC-I to -III scores of cells across the three young and aged single-cell RNA-seq samples. Only ISC-II score is affected by age.

observed that ageing resulted in distinct signaling pathway changes across the individual cell types (Figure 2D). For example, fatty acid metabolism, which has been linked to intestinal ageing,[12] was enriched in aged enterocyte progenitors and enterocytes, while diminished in TA cells, EECs, and GCs. In contrast, inflammation-associated pathways of the *Inflammaging gene set* were enriched during ageing across all cell types. To resolve the inflammaging expression signature further to the single-cell level, we calculated an *Inflammaging score* per individual cell. For this, we aggregated the expression levels for all genes of the *Inflammaging gene set* and compared them with a random set of 100 genes with similar expression levels. We plotted the score for every single cell of the young and aged intestines separately in a tSNE visualization (Figure 2E). This analysis identified that in young tissue, ISCs, PCs, and TA cells in the intestinal crypt have a lower level of tonic inflammatory signaling than the cell types located above the crypt (Figure 2E), while upon ageing, the inflammatory status is clearly elevated in all cell types of the intestinal epithelium (Figures 2E and 2F). These results demonstrate that while inflammaging establishes differently in cells along the crypt-villus axis, it affects all cell types of the aged intestinal epithelium (Figure 2G).

## MHC-II upregulation as a hallmark of inflammaging in aged ISCs

ISCs are highly proliferative and constantly renew the entire epithelium every few days. Thus, ISCs are most critical for tissue homeostasis and especially susceptible to the manifestation of ageing phenotypes. To determine the impact of inflammaging on ISCs, we focused our analysis on the DEGs of the stem cell cluster. Among the 91 DEGs in aged ISCs, we identified the interferon-inducible gene *Ly6e* as the most significantly upregulated gene, alongside many MHC-II-encoding genes as well as *Ciita*, the transcriptional activator of MHC-II (Figures 3A and 3B). Generally, MHC-II molecules function on the cell surface by antigen presentation to CD4$^+$ T cells,[24] and a recent study demonstrated that ISCs functionally present antigens to CD4$^+$ T cells via MHC-II.[10] To assess the functional relevance of increased transcript levels of MHC-II-encoding genes in aged ISCs, we measured MHC-II proteins on the cell surface of Lgr5$^+$ ISCs

from young and aged mice. We detected a significant gain in MHC-II-derived signal on the surface of aged Lgr5$^+$ ISCs compared with that of young ISCs (Figure 3C). Thus, aged ISCs are marked by the upregulation of MHC-IIs, which are functionally located at the stem cells' surface, suggesting an increased potential for aged stem cells to interact with CD4$^+$ T cells. In a previous study, young Lgr5$^+$ ISCs were partitioned into three subsets (ISC-I–III) based on their expression of factors known to interact with immune cells, including MHC-II.[10] Importantly, different stem cell characteristics were identified for the three ISC subsets. While stem cells in the ISC-I subset are low cycling and display most stem-like features, ISC-II and -III are more proliferative and progressively more differentiated. To test whether aged ISCs represent a higher overlap with one of these subsets, indicating a change in stem cell biology upon ageing, we scored the transcriptomes of our young and aged ISCs by their similarity to the three ISC subsets. Unsupervised clustering of ISCs showed a clear separation of young and aged cells (Figure 3D), and aged stem cells displayed high ISC-II scores compared with young ISCs (Figures 3D and 3E). In comparison, ISC-I and -III scores were not changed between young and aged cells (Figure 3E), indicating that aged ISCs shift toward a progressively more differentiated state with less stem-like features.

## Increased MHC-II levels on aged ISCs are associated with elevated numbers and interactions with CD4$^+$ T cells

In order to address whether increased MHC-II levels on aged ISCs could mediate cellular interactions with surrounding immune cells that provide extrinsic signals to the epithelium and drive inflammaging, we investigated the ageing immune microenvironment. To this end, we performed 20-plex spectral flow cytometry on cells of the proximal small intestine of young and aged Lgr5-EGFP reporter mice,[6] enabling the quantification of all major immune cell populations at a single-cell level (Figure 4A). Clustering and dimensionality reduction of the recorded data allowed for distinction between CD45$^+$ immune cells and EPCAM$^+$ epithelial cells (Figure 4A). On the basis of known cell-type markers, we defined 12 different immune cell types within the CD45$^+$ population (Figures 4B and S3A–S3H). Stratifying the analysis by the age of the mice indicated an enrichment of CD4$^+$ and CD4$^+$ CD8$^+$ TCR$\alpha\beta^+$ T cells in the ageing intestine (Figures 4B and 4C). Further analysis identified a clear shift in the TCR$\alpha\beta^+$ T cell subtypes (Figure 4D). During ageing, the proportion of CD4$^+$ and CD4$^+$ CD8$^+$ T cells markedly increased from approximately 5%–10% of all TCR$\alpha\beta^+$ T cells, in accordance with previously reported proportions of intraepithelial lymphocytes,[25] to up to 25%–30% at the expense of CD8$^+$ T cells. On the basis of the described interaction of ISCs with CD4$^+$ T cells via MHC-II,[10] we hypothesized that elevated MHC-II levels on ISCs might act as hub for increased ISC-CD4$^+$ T cell interactions. To test this, we quantified the abundance of potentially interacting cells by gating on CD45$^+$ EPCAM$^+$ double-positive heterotypic cell events[26] and further gated this population for CD4$^+$, TCR$\beta^+$, and Lgr5$^+$ (Figure S3I). This unveiled CD4 and Lgr5 double-positive events, indicating physically interacting ISCs and CD4$^+$ T cells. To further verify this interaction, we used the previous surface markers to gate double-positive cells (Figures S3I and S3J) and simultaneously captured images of these events by image flow cytometry. This allowed us to directly visualize the ISC-CD4$^+$ T cell interaction pairs by flow cytometry (Figures 4E and S3K). IHC and immunofluorescence staining of small intestinal tissue sections further supported the existence of these interaction events *in vivo* (Figures 4F and S3L). Examining our spectral flow cytometry data, we found a tendency of increased interaction between Lgr5$^+$ ISC and CD4$^+$ TCR$\beta^+$ T cells in aged mice (Figure 4G). Probing our scRNA-seq data, we could also rule out an elevated co-occurrence of *Cd4* and *Lgr5* gene expression in cells of the intestine upon ageing (Figures S1K and S1L), which could have confounded our initial analysis.

In the ageing immune microenvironment, we detected elevated levels of PD-1 and PD-L1 (Figures S3M and S3N), indicators of T cell activation and exhaustion[27] as well as of FOXP3$^+$ regulatory T cells (Figure S3O), which have a central role during immunological homeostasis.[28] Overall, these indicate a disbalance in immune homeostasis in the intestine upon ageing.

Taken together, our data show that the ageing immune microenvironment undergoes substantial changes, which include a shift in TCR$\alpha\beta^+$ T cell subtypes, resulting in elevated numbers of CD4$^+$ T cells. This alteration is associated with a trend toward an increased frequency of physical interaction between aged ISCs, which themselves have higher MHC-II levels, and CD4$^+$ T cells. As T cells are a major source of IFN-$\gamma$ and other inflammatory mediators, this interaction may represent an extrinsic source to promote inflammaging in aged ISCs and IECs.

## Aged ISCs propagate cell-intrinsic sources of inflammaging in intestinal organoids

Next, we aimed to decipher whether the inflammaging phenotype is mainly driven by direct interaction with the microenvironment, such as surrounding immune cells, or whether stem cells also acquire intrinsic sources of inflammaging. To this end, we assessed transcriptional changes in small intestinal organoids[29] that were generated from young and aged mice of 2–3 and 20–22 months, respectively (hereafter referred to as young and aged organoids) by bulk RNA-seq of six different organoid lines per age (Figure 5A). Prolonged culture period ensured immune-cell-free organoid cultures, as confirmed by our sequencing results, in which we could not detect *Cd45*, a pan hematopoietic cell marker. Therefore, recurrent passaging and renewal of organoid cultures from a limited population of ISCs should allow for the identification of age-related changes that are manifested intrinsic to ISCs during ageing, are propagated to progenitor cells, and are independent of immune cells.

First, we aimed to ascertain how well organoid cultures recapitulate the *in vivo* ageing phenotype. In a PCA, the age of the mice from which the organoids were generated was the first driving force to separate the samples (Figure 5B). This clear separation of *ex vivo* cultures by their age indicated that age-related transcriptional changes persist in culture for at least several weeks, independent of direct signals from the microenvironment. In total, we identified 599 genes significantly differentially expressed with age (Figure S4A), of which 147 genes overlapped with those detected *in vivo* (Figures S4B and S4C; Table S2). Within these 140 DEGs, we identified genes involved in the immune response as upregulated during ageing, such as *Ly6e*, *Ccr2*, *Ifitm3*, *P2rx7*, and *Tnf* (Figure 5C). When we analyzed the *in vivo* and *ex vivo* bulk RNA-seq datasets together, we observed

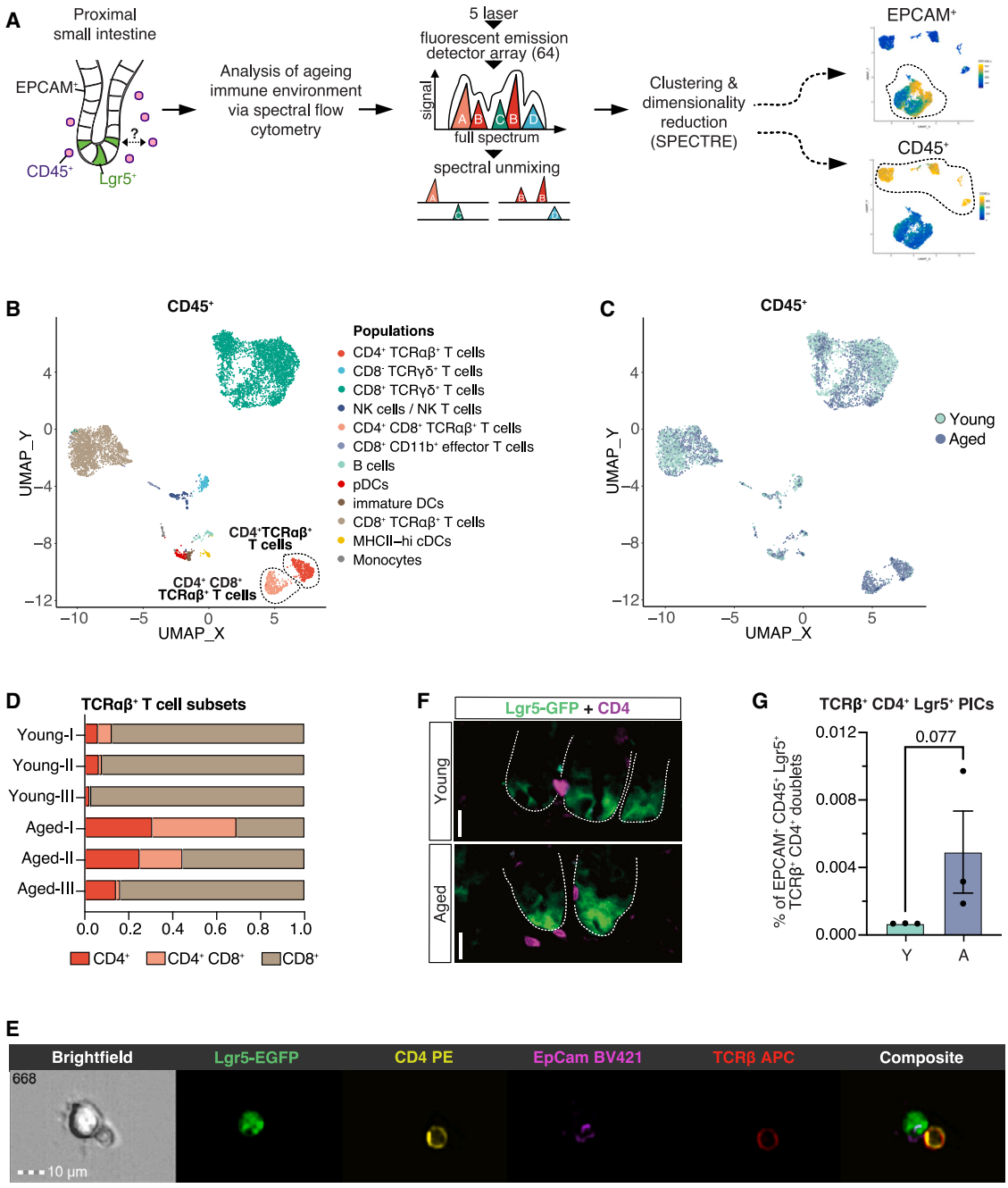


**Figure 4. Increased MHC-II levels on aged ISCs are associated with elevated numbers and interactions with CD4$^+$ T cells**

(A) Experimental scheme for spectral flow analysis of the ageing intestinal immune microenvironment. Cells were split into CD45$^+$ hematopoietic cells and EPCAM$^+$ epithelial cells for downstream analysis.

(B) Representative UMAP display of surface measurements of single CD45$^+$ hematopoietic cells from young and aged mice as described in (A). Colors indicate different cell types. 2,000 random cells from each of 3 young and aged mice are shown.

(C) UMAP from (B), colors indicate cells derived from young or aged mice

(D) Quantification of TCRαβ$^+$ T cells in the intestine of individual mice by flow cytometry.

(E) CD4$^+$/Lgr5$^+$ interaction pairs, visualized as Lgr5-EGFP-, EpCam-BV421- and CD4-PE-, TRCβ-APC-positive cells by imaging flow cytometry.

(F) Composites of immunofluorescence staining against CD4 and GFP in the small intestine of Lgr5-EGFP mice. Intestinal crypts are highlighted with white dashed lines; scale bars, 25 µm.

(G) Quantification of TCRαβ$^+$ CD4$^+$ Lgr5$^+$ cells out of CD45$^+$ EPCAM$^+$ double-positive heterotypic cell events as a percentage from all analyzed events. Data are represented as mean ± SEM and data points represent the results biological replicates. Statistical significance was tested by a Wilcoxon rank-sum test, p = 0.077.

See also Figures S1 and S3.

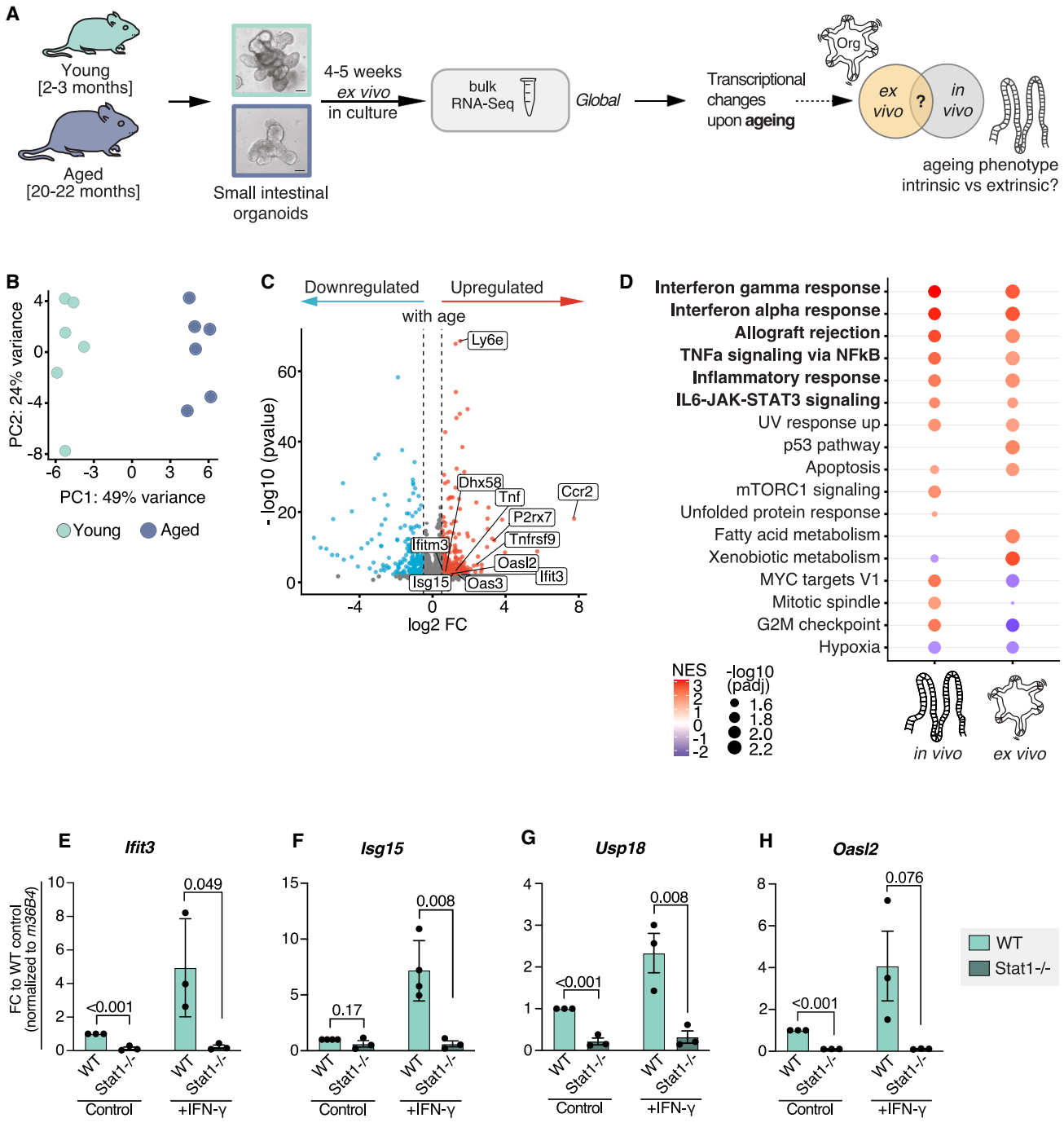


**Figure 5. Aged ISCs propagate cell-intrinsic sources of inflammaging in intestinal organoids**

(A) Schematic of the experimental approach of bulk RNA-seq of small intestinal organoids.

(B) Principal-component analysis identifies the age of the mice (young, n = 6; aged, n = 6) from which the organoids were generated as the first driving force to separate the samples based on transcriptional changes.

(C) Volcano plot showing differentially expressed genes upon ageing (aged over young) in small intestinal organoids; red, significantly (FDR ≤ 10%) upregulated ($log_2$ FC > 0.5); blue, significantly downregulated ($log_2$ FC < [−0.5]); gray, not significantly changed and absolute $log_2$ FC < 0.5.

(D) Gene set enrichment analysis with side-by-side comparison of *in vivo* (left) and *ex vivo* (right) normalized enrichment score (NES); filtered for FDR of ≤5%.

(E–H) Transcriptional changes of (E) *Ifit3*, (F) *Isg15*, (G) *Usp18*, and (H) *Oasl2* in wild-type (WT) and Stat1 knockout (Stat1$^{-/-}$) organoids in control and IFN-γ (500 pg/ml, 6 h) treatment conditions. Transcript levels were assessed by quantitative real-time PCR (normalized to 36B4) in n = 3 biological replicates per age and treatment and calculated as fold change (FC) compared with the WT control condition. Data are represented as mean ± SD, and data points represent the results of biological replicates. Statistical significance was tested by an unpaired t test (two-sided).

See also Figures S4 and S5 and Table S2.

a strong correlation between age-dependent DEGs (Figure S4D) and identified a stable age effect across all samples (Figures S4E and S4F). To further assess the overlap of age-related transcriptional changes between intestinal organoids and *in vivo* intestinal epithelium from a functional perspective, we compared the enriched gene sets between both bulk RNA-seq experiments. Notably, this analysis identified an enrichment for all six pathways previously defined as *Inflammaging gene set* in aged organoids (Figure 5D). In addition to the *Inflammaging gene set*, other pathways showed overlapping differential expression. For example, UV-response- and apoptosis-associated genes were upregulated, while hypoxia-associated genes were downregulated. Other pathways, such as the unfolded protein response or mTORC1 signaling, were exclusively enriched *in vivo*. From this, we concluded that organoids maintain some ageing phenotypes in culture, including the inflammaging phenotype of the aged intestinal epithelium, which is partially maintained in culture and persists even for a prolonged time of up to ten passages (Figures S4G and S4H).

To gain insight into the mechanism of the inflammaging phenotype, we examined the responsiveness and dependence of inflammaging genes on the IFN signaling pathway. As STAT1 functions as a major transcriptional regulator for IFN signaling pathways I and II,[30,31] we generated organoids from a Stat1 knockout (KO) mouse model[30] and assessed the expression of inflammaging genes at the baseline state and upon IFN-γ stimulation (Figures 5E–5H, S4I, and S4J). At baseline, the expression of *Ifitm3*, *Ifit3*, *Oasl2*, and *Usp18* was significantly lowered in Stat1 KO compared with wild-type (WT) organoids, identifying a general dependence of these genes on STAT1 signaling in the intestinal epithelium. After 6 h of IFN-γ stimulation, WT organoids showed a 2.5- to 7-fold induction of gene expression, whereas Stat1 KO organoids showed no response to IFN-γ, demonstrating the dependence of genes of the inflammaging signature on STAT1 signaling.

Next, we targeted NF-κB signaling, which had also shown an enrichment upon ageing. We treated organoids with TPCA-1 (Figures S4K–S4O), a known IKKβ antagonist that primarily inhibits NF-κB signaling.[32,33] TPCA-1 has been shown to have anti-inflammatory effects in an identity by descent (IBD) model by reducing the secretion of inflammatory cytokines, including CXCL10.[32] We observed a robust downregulation of *Cxcl10* expression upon TPCA-1 treatment in young and aged organoids (Figure S4L), confirming its efficient inhibitory function. *Isg15* and *Oasl2* were significantly downregulated by TPCA-1 in aged organoids to similar levels as observed in young ones (Figures S4M and S4N). However, we did not observe such an effect for *Ly6e*, which TPCA-1 did not reduce in young or aged organoids (Figure S4O).

In summary, epithelial cells develop an intrinsic inflammatory signature during ageing that persists in culture even in the absence of direct signals from the immune microenvironment. Mechanistically, the expression of inflammaging signature genes is dependent on STAT1 signaling. Moreover, the expression of some inflammatory genes can be attenuated by inhibition of the NF-κB pathway. Since organoid cultures are repeatedly renewed from a limited population of ISCs, these results suggest that the inflammaging signature manifests intrinsic to ISCs during ageing and is propagated to newly arising cells of the organoids.

### ISC-intrinsic inflammaging is primed on chromatin level

Next, we aimed to determine how cell-intrinsic inflammaging is maintained in culture without signals from the microenvironment. In the context of ageing, senescence-associated secretory phenotype (SASP) is a known potential source of cytokines that trigger inflammatory responses.[34] We detected SASP-associated cytokines secreted by organoids, but these showed no significant difference between the two age groups (Figures S5A–S5D). Furthermore, our bulk RNA-seq data also did not indicate a senescence phenotype. To extend our analysis to all secreted factors, we performed a functional secretome assay (Figure S5E). Here, young organoids were exposed to the secretome of aged organoids (A>Y) for 3, 6, or 24 h, and the expression of inflammaging genes (*Ly6e*, *Isg15*, *Ifit3*) was subsequently measured. Young organoids that were exposed to the secretome of young organoids (Y>Y) served as reference controls. We observed that the expression levels of the tested inflammatory genes in young organoids that were exposed to secretome of aged organoids are not higher than those in young-organoid-secreted factors (Figures S5F–S5H). From the results of the cytokine measurement and functional secretome assay, we concluded that secreted factors are unlikely to promote the inflammaging signature in aged organoids.

Previously a study on mouse tissue showed that ageing in the liver, heart, and neural lineage was associated with an inflammatory response accompanied by epigenetic remodeling.[35] Therefore, we asked whether epigenetic changes could underlie the inflammation-associated transcriptional changes observed in the aged small intestinal epithelium *in vivo* and explain how this transcriptional profile is maintained over weeks *ex vivo*. To test this hypothesis, we assessed changes in chromatin accessibility in young and aged small intestinal organoids by Assay for Transposase-Accessible Chromatin with high-throughput sequencing (ATAC-seq).[36] As expected, the majority of annotated peaks identified were located mainly in distal intergenic (30%) and promoter (26%) regions (Figure S6A). Remarkably, PCA showed a clear separation of young and aged samples based on open chromatin sites (Figure 6A). This demonstrated that chromatin accessibility changes upon ageing in IECs and that many of these changes are maintained in culture for at least several weeks. Differential accessible region analysis identified 2,442 peaks that changed significantly during ageing (Figure S6B). For example, we detected increased chromatin accessibility for *Ccr2*, *Ly6e*, and *Dhx58* (Figures 6B, S6C, and S6D), which are associated with immune response and inflammation and were also transcriptionally upregulated in aged organoids (Figure 5C). To investigate the mechanism that drives inflammaging in aged ISCs and progenitors, we assessed transcription factor (TF) binding sites enriched on age-dependent open chromatin regions. The enrichment analysis for genomic loci (*Locus Overlap Analysis*, LOLA)[37] showed an increased frequency of peaks associated with Stat1 and Rela, TFs that mediate immune and inflammatory responses (Figure S6E). Next, we plotted the significant DEGs of bulk RNA-seq against the significant peaks of the ATAC-seq and highlighted all genes belonging to our *Inflammaging gene set* (Figure 6C). This analysis identified that the transcriptional changes during ageing and the differentially accessible regulatory regions correlated with each other and showed the same directionality in their regulation. For example, *Ccr2* showed increased chromatin accessibility in aged organoids, which coincided with transcriptional upregulation

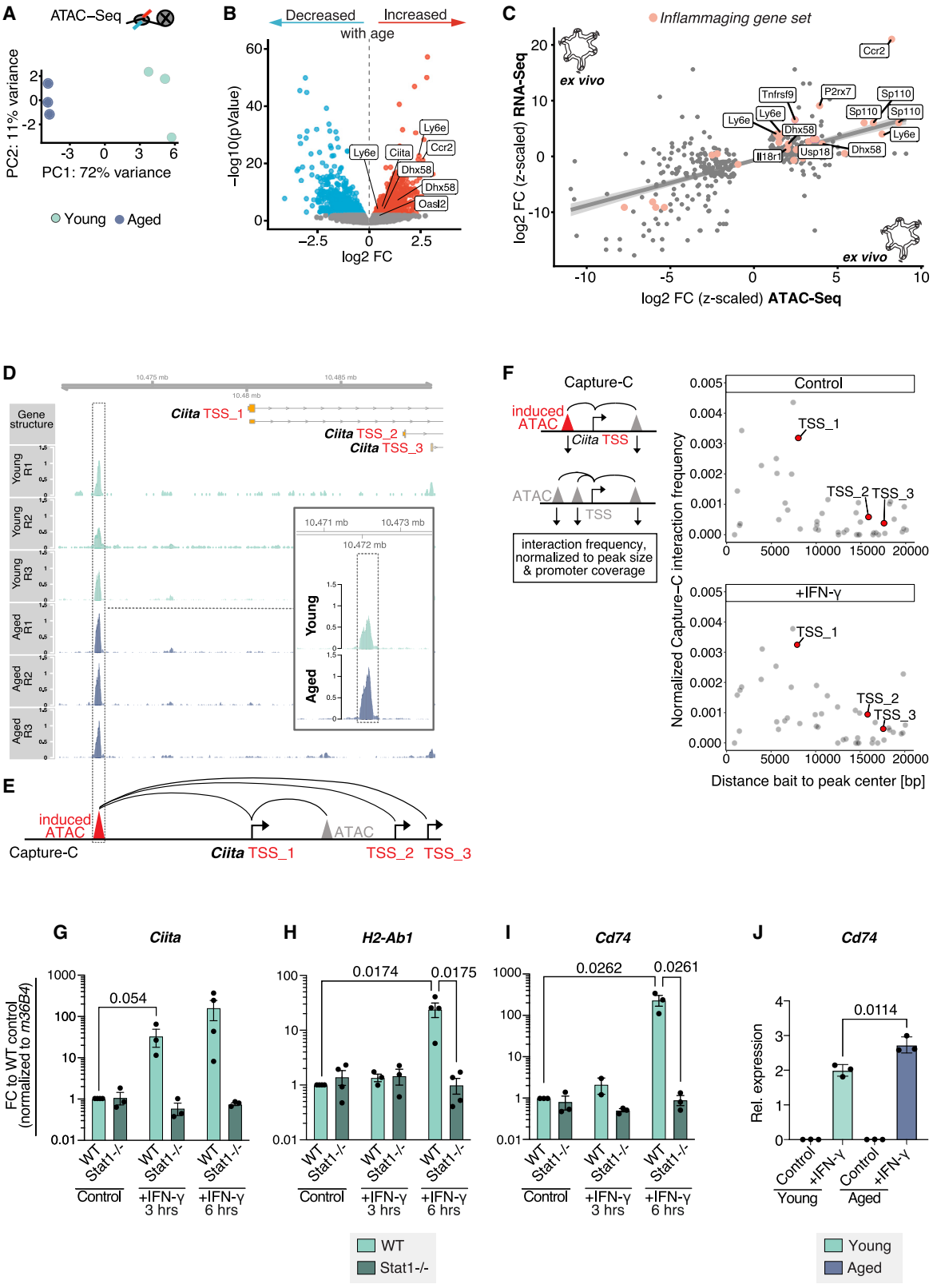


**Figure 6. ISC-intrinsic inflammaging is primed on the chromatin level**

(A) Chromatin accessibility in young and aged organoids was determined by ATAC-seq. PCA identifies the age of the mice (young: n = 3, aged: n = 3), from which the organoids were generated, as the first driving force to separate the samples.

*(legend continued on next page)*

during ageing (Figures 5C and 6B). Importantly, many genes that showed a similar trend to *Ccr2* belonged to the *Inflammaging gene set*, including *Ly6e*, *P2rx7*, *Usp18*, *Il18r1*, and *Tnfrsf9* (Figures 6C, 7D, 7E, S6C, and S6D), supporting our hypothesis that cell-intrinsic inflammaging is associated with chromatin remodeling. Based on the stem cell-dependent properties of intestinal organoids, these results suggest that age-associated chromatin remodeling manifests in aged ISCs and is transmitted to progenitor cells and therefore stable in culture over several weeks.

To test how the chromatin landscape from aged organoids would correlate with the age-dependent transcriptional changes of the *in vivo* epithelium, we plotted the significant peaks of the organoid ATAC-seq against the DEGs from the *in vivo* bulk RNA-seq experiment (Figure S6F). We observed a correlation between our bulk RNA-seq and ATAC-seq data, including genes of the *Inflammaging gene set*, suggesting that the elevated chromatin accessibility in the aged intestinal epithelium provides a permissive state for inflammatory signaling, and this epigenetic potential may be further exploited *in vivo*.

Interestingly, we also discovered in aged organoids a regulatory region with increased chromatin accessibility for *Ciita* (Figures 6B and 6D), the MHC-II transactivator that was strongly upregulated *in vivo* upon ageing (Figures 1B, 1C, 3A, and 3B). This finding piqued our interest because the expression of MHC-II-encoding genes is strongly reduced in culture, whereas co-culture with immune cells or direct treatment with IFN-γ has been shown to restore MHC-II expression.[10] To assess whether IFN-γ treatment also induces *Ciita* expression in the intestinal epithelium, we treated intestinal organoids with IFN-γ and monitored the expression of *Ciita* and MHC-II genes *H2-Ab1* and *Cd74* over time (Figures 6G–6I). This identified a transcriptional induction of *Ciita* by approximately 30-fold as early as 3 h after treatment and a robust induction of *H2-Ab1* and *Cd74* after 6 h, reflecting the signaling dynamics of *Ciita* as MHC-II transactivator. Using Stat1 KO organoids,[30] we further demonstrated that the induction of *Ciita* and MHC-II genes by IFN-γ is strongly STAT1 dependent (Figures 6G–6I). To ascertain whether the induced ATAC peak 7 kb upstream of the first transcriptional start site (TSS_1) of *Ciita* (as highlighted in Figures 6D and 6E) is indeed regulatory for its gene expression and possibly involved in IFN-γ-mediated transcriptional activation of *Ciita*, we examined the spatial proximity between this ATAC peak and the three TSSs of *Ciita* by low-input Capture-C[38] in aged control organoids after IFN-γ treatment. In control and IFN-γ-treated organoids, this approach demonstrated an enrichment in interaction frequency of the induced ATAC peak with *Ciita* TSS_1 compared with other promoter interactions with ATAC peaks within a 20-kb upstream and downstream radius, including *Ciita* TSS_2 and TSS_3 (Figure 6F). Importantly, the increased interaction frequency was observed independently of the total interaction frequency of the *Ciita* promoter (Figure S6G). Thus, our analysis strongly suggests that organoids exhibit age-related increased chromatin accessibility in a regulatory region of *Ciita*, indicating that *Ciita* possesses an increased epigenetic potential[39] for enhanced stimulation in aged IECs, which stays unexploited in culture due to the lack of extrinsic signals. *In vivo*, however, interaction with cells in the microenvironment, for example, IFN-γ-secreting immune cells, could trigger this primed potential. To test this increased sensitivity of MHC-II upon extrinsic stimulation, we treated organoids with IFN-γ, a key cytokine of $CD4^+$ T cells, which are known to interact with ISCs (Figures 4E–4G and Biton et al.[10]). Indeed, IFN-γ treatment resulted in a more elevated transcriptional induction of the MHC-II genes *Cd74* and *H2-Ab1* in aged organoids than in young organoids (Figures 6J and S6H).

In summary, we identified an increase in open chromatin in inflammation-associated loci in aged ISCs and progenitors in *ex vivo* organoid cultures. These chromatin changes appear to be maintained in ISCs, being stable over several weeks in culture, and may underlie the intrinsic inflammaging signature of aged organoids. Our results also indicate that aged IECs harbor an increased epigenetic potential for inflammatory responses, which may be exploited by signals from the immune microenvironment, such as IFN-γ, a key cytokine of $CD4^+$ T cells.

## Changes in chromatin accessibility in the aged intestinal epithelium are established *in vivo* and maintained *ex vivo*

To determine whether age-related changes in chromatin accessibility, as observed in organoid cultures, are already established

(B) Volcano plot showing significantly (FDR ≤ 10%) changed peaks of chromatin accessibility in genetic regions/loci upon ageing (aged over young) in small intestinal organoids derived from young (n = 3) and aged (n = 3) mice; red, increased ($log_2$ FC > 0); blue, reduced ($log_2$ FC < 0); gray, not significantly changed.
(C) Scatterplot of the effects of ageing on the expression of genes as determined by bulk RNA-seq of intestinal organoids (y axis, z-scaled $log_2$ FC) and on the chromatin accessibility as determined by ATAC-seq in intestinal organoids (x axis, z-scaled $log_2$ FC). Genes of the inflammaging gene set are color highlighted, and a linear regression line indicates the agreement between the compared datasets (95% CI shaded gray). Only genes significantly (FDR ≤ 10%) affected are included.
(D) Peak density in the regulatory region assigned to *Ciita* as assessed in intestinal organoids is shown for all young (n = 3) and aged (n = 3) samples in genomic coordinates close to *Ciita* by R/Gviz. Inlet shows aggregated peak densities per age.
(E) Schematic Capture-C approach: interaction of *Ciita* TSS_1–3 and other control gene promoters (listed in Table S4) with the induced ATAC peak (Figure 6D) and other ATAC peaks in a 20-kb radius was assessed.
(F) Normalized Capture-C interaction frequencies between ATAC peaks and gene promoters, plotted by the distance of peak center to promoter-overlapping bait center (bait: Capture-C probes designed against promoters of *Ciita* TSS_1–3 + control genes; Table S4) for control (top) and IFN-γ-treated (bottom) organoids. Red dots represent interactions of the induced ATAC peak highlighted in (D) and (E) with *Ciita* TSS_1–3 (as annotated in D and E).
(G–I) Transcriptional changes of (F) *Ciita*, (G) *H2-Ab1*, and (H) *Cd74* in wild-type (WT) and Stat1 knockout ($Stat1^{-/-}$) organoids in control and IFN-γ-treated (500 pg/ml) organoids (3 and 6 h). Transcript levels are shown in log scale and were assessed by quantitative real-time PCR (normalized to 36B4) in n = 3 biological replicates per age and treatment and calculated as fold change (FC) compared with the WT control condition. Data are represented as mean ± SD, and data points represent the results of biological replicates. Statistical significance was tested by an unpaired t test (two-sided).
(J) Transcriptional changes of *Cd74* in young and aged organoids in control or IFN-γ treatment (2 ng/ml) conditions. Transcript levels assessed by quantitative real-time PCR (normalized to *36B4*) in n = 3 biological replicates per age and treatment. Data are represented as mean ± SD and data points represent the results biological replicates.
See also Figure S6.

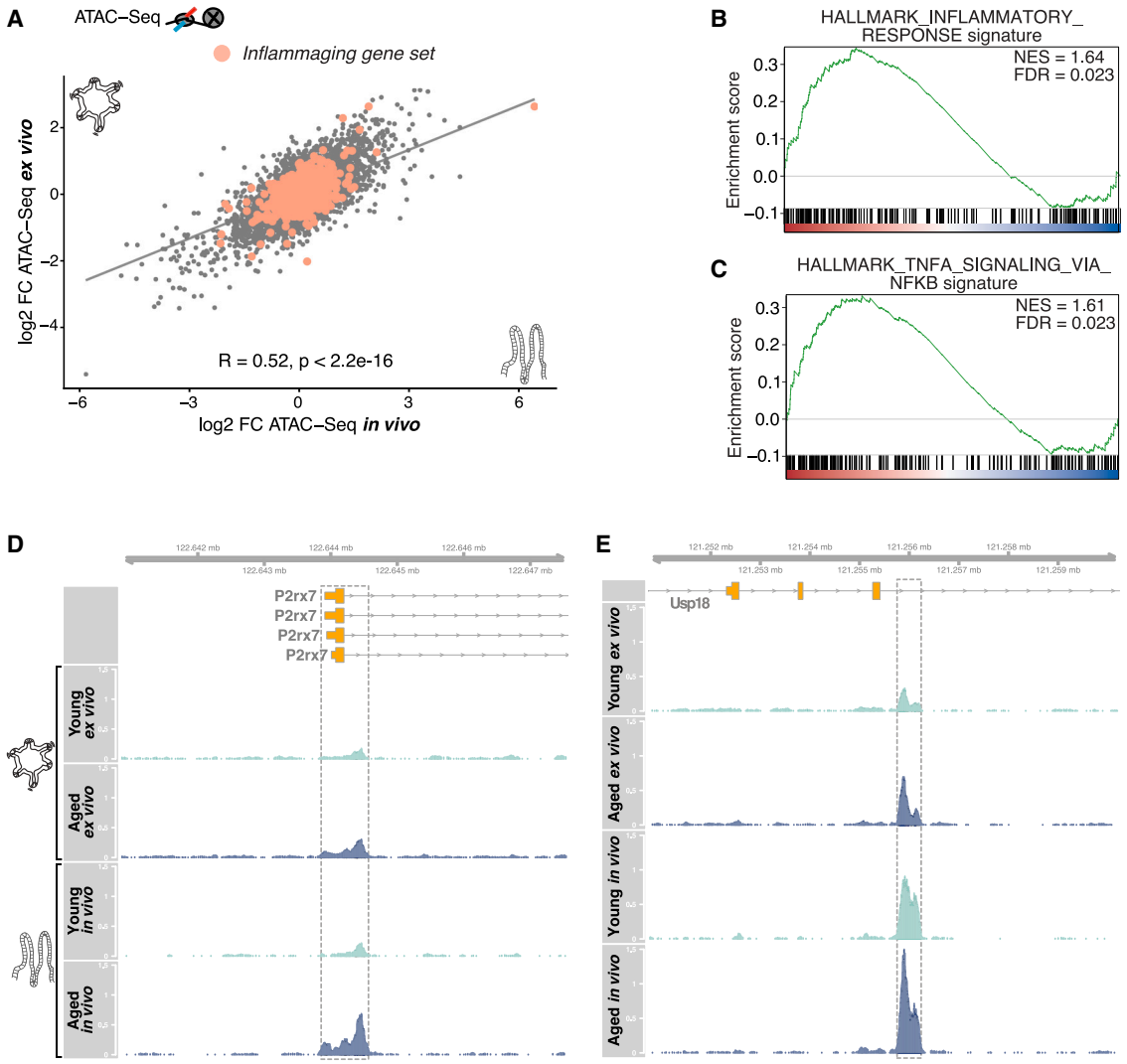


**Figure 7. Age-related chromatin remodeling in the intestinal epithelium is established *in vivo* and maintained *ex vivo***

(A) Scatterplot of the effects of ageing on chromatin accessibility as determined by ATAC-seq of intestinal organoids (y axis, $log_2$ FC) and *in vivo* intestinal epithelium (x axis, $log_2$ FC). Genes of the inflammaging gene set are color highlighted. A linear regression line indicates the agreement between the compared datasets. Pearson correlation coefficient R and a p value (p) of a test for correlation are shown. All genes (irrespective of FDR) are included.

(B and C) Gene set enrichment analysis based on age-related changes in chromatin accessibility of freshly isolated *in vivo* intestinal epithelium. Normalized enrichment score (NES) based on gene set enrichment analysis on hallmark gene sets (MSigDB) and respective FDR are shown. The barcode indicates the position of gene-associated loci from the respective pathway according to their expression level (left/red, increased; right/blue, decreased).

(D and E) Peak density in the regulatory region assigned to (D) *P2rx7* and (E) *Usp18* as assessed in *ex vivo* intestinal organoids and freshly isolated *in vivo* intestinal epithelium is shown as aggregated peaks for all young (n = 3) and aged (n = 3) samples in genomic coordinates close to respective gene bodies by R/Gviz.

See also Figure S7.

*in vivo* and then maintained *ex vivo* and do not display a culture artifact, we performed ATAC-seq from freshly isolated IECs from young and aged mice. As previously observed in organoid cultures, the majority of annotated peaks identified were located mainly in distal intergenic (30%) and promoter (29%) regions (Figure S7A). When we analyzed the *in vivo* and *ex vivo* ATAC-seq datasets together, we identified a stable age effect across all samples (Figure S7B). This indicated that age-related changes in chromatin accessibility of IECs are indeed established *in vivo* and are retained in culture. In line, the differentially accessible regulatory regions determined in freshly isolated epithelial cells and *ex vivo* organoid cultures upon ageing showed a high correlation (R = 0.52, p < 2.2e−16) (Figure 7A), and many of the significantly differential ATAC peaks belonged to our *Inflammaging gene set* (Figures 7A, 7D, 7E, and S7C). This finding was confirmed by GSEA of the *in vivo* ATAC-seq dataset, which identified enrichment for inflammatory response and TNF-α signaling via NF-κB signatures upon ageing (Figures 7B and BC), as previously detected in transcriptional changes in *in vivo* and *ex vivo* samples (Figures 2D and 5D). In addition, analysis of transcription factor motifs on age-related changes in chromatin accessibility in our *in vivo* ATAC-seq dataset identified significant enrichment for the binding motif of the TF Jun

(Figures S8D and S7E), which has been shown to be involved in establishing an inflammatory memory in epidermal skin cells.[40]

In summary, age-related changes in chromatin accessibility, including those at inflammation-associated loci, are established in the intestinal epithelium during ageing *in vivo* and largely maintained in *ex vivo* organoid cultures.

## DISCUSSION

In this study, we aimed to dissect cell-intrinsic and -extrinsic sources of chronic inflammatory signaling during ageing, known as inflammaging, in the mouse small intestinal epithelium.

Previous studies have described inflammation in the aged intestine, either on tissue level or in isolated crypts.[16,17] Using scRNA-seq, we were able to resolve the inflammaging phenotype down to a single-cell level of the intestinal epithelium and to define how it manifests differently along the crypt-villus axis. Interestingly, at a young age, the basal, low-level expression of inflammation-related genes was lower in cells of the intestinal crypt than in cells along the villi, in line with a previous report showing that the crypt structure shields ISCs from microbiota and external stimuli.[41] However, the establishment of the inflammaging phenotype in aged cells appeared to be less dependent on their location along the crypt-villus axis, indicating that extrinsic signals are not the only factors to determine the inflammaging phenotype.

In aged ISCs, we identified a strong upregulation of MHC-II molecules, which mediate antigen presentation to $CD4^+$ T cells. The functional role of MHC-II on epithelial cells has just recently started to be explored in more detail. MHC-IIs on lung epithelial cells were shown to be involved in maintaining barrier immunity and shaping the immune response.[42] In the intestine, ISC-$CD4^+$ T cell interactions via MHC-II are instructive for ISC differentiation and renewal, and MHC-II expression on ISCs is important for an efficient response during infection.[10] In addition, high-fat-diet-induced reduction of MHC-II levels on ISCs can enhance intestinal tumorigenesis.[43] In our study, the strong upregulation of MHC-II in ISCs during ageing was associated with an increased frequency of $CD4^+$ $TCR\beta^+$ T cells and a trend toward increased physical interaction between ISCs and $CD4^+$ T cells. These findings allow hypothesizing that elevated levels of MHC-II on aged ISCs may promote epithelial inflammaging by attracting $CD4^+$ T cells that secrete IFN-$\gamma$ and other extrinsic inflammatory signals. Moreover, the data suggest that during ageing, a feedforward loop might manifest in the intestine: the increase in MHC-II levels, antigen presentation, and attraction of $CD4^+$ T cells leads to elevated $CD4^+$ T cells numbers and secretion of IFN-$\gamma$ to ISCs, which in turn strongly induce MHC-II expression, as demonstrated in our organoid treatment experiments. Elucidating the chronology of these events will be an important aspect of future work and provide fundamental insights for developing anti-inflammatory interventions.

Ageing phenotypes observed *in vivo* display the result of crosstalk between many different cell types, making it difficult to dissect cell-intrinsic from -extrinsic effects. To disentangle the inflammaging phenotype, we exploited the *ex vivo* intestinal organoid cultures, which are renewed every few days from a limited ISC population. In aged organoids, we detected a stable age effect that persisted over weeks in culture, including an inflammaging phenotype in the absence of surrounding immune cells as an inflammatory trigger. To identify how aged intestinal organoids maintain the inflammaging signature in the absence of immune cells, we assessed open chromatin sites in our organoid cultures. The organization of the epigenome and transcriptome undergoes substantial changes upon ageing, as demonstrated in a set of murine organs, not including the small intestine.[35,44] In our study, we show that age-related changes in chromatin accessibility are established already *in vivo* and maintained in *ex vivo* organoid cultures, thus independent of extrinsic signals from the microenvironment. Moreover, the ISC-intrinsic inflammaging signature coincides with increased chromatin accessibility in inflammation-associated loci, indicating that the ISC-intrinsic inflammaging is primed at the chromatin level, reminiscent of memory of inflammation in epithelial stem cells.[45] Future work will be required to identify what underlies the remodeling of the chromatin status at these genomic regions and if, for example, recurrent infections over a lifetime could enhance these modulations.

In addition to infections, age-related changes in the microbiome may be involved in the inflammaging phenotype. Inflammation can favor the colonization of pathobionts, which in turn can displace beneficial symbionts, for example, short-chain fatty acid (SCFA)-producing microbes.[46] Since SCFAs have anti-inflammatory functions, their decline in the intestinal mucosa may further exacerbate the inflammatory phenotype, creating a self-perpetuating cycle.

In summary, we provide evidence for stem cell-intrinsic sources of inflammaging. In addition, our data point to an extrinsic source, represented by IFN-$\gamma$ secreted by $CD4^+$ T cells inducing MHC-IIs and genes of the inflammaging signature via STAT1 signaling. These two sources may well act in parallel. Whether they are linked, for example, so that elevated IFN-$\gamma$ levels in *in vivo* intestinal tissue are involved in the development of the cell-intrinsic inflammaging signature, is an interesting question for future experiments, as is the possible involvement of the microbiome.

### Limitations of the study

Our study identifies stem cell-intrinsic sources of inflammaging that are associated with chromatin remodeling at inflammation-associated loci upon ageing. While we were able to exclude secreted factors as major driver to sustain the inflammatory signaling in culture, we cannot rule out that additional processes, such as deregulated endogenous retroviruses, or the microbiome are at play to facilitate age-related inflammation in the intestinal epithelium.

In addition to cell-intrinsic sources, our data provide evidence for an extrinsic source of inflammatory signaling, represented by $CD4^+$ T cell-secreted IFN-$\gamma$, which induces MHC-IIs and genes of the inflammaging signature. While IFN signaling may well be involved in the chromatin remodeling in aged epithelial cells, our study could not directly link both sources of inflammatory signaling.

## STAR★METHODS

Detailed methods are provided in the online version of this paper and include the following:

- KEY RESOURCES TABLE

## SUPPLEMENTAL INFORMATION

Supplemental information can be found online at https://doi.org/10.1016/j.devcel.2023.11.013.

## ACKNOWLEDGMENTS

We are grateful to Fillip Port, Kim E. Boonekamp, Siamak Redhai, Christian Scheeder, Josephine Bageritz, and the rest of the Boutros lab for valuable discussions. We thank Marieke Essers for providing Stat1 knockout mice and Annette Kopp-Schneider of the Department of Biostatistics for statistical advice. We thank Katharina Bauer and Jan-Philipp Mallm from the DKFZ single-cell open lab and DKFZ Flow cytometry CF for support with single-cell RNA-seq experiments, as well as the DKFZ Genomics and proteomics CF for support in sequencing bulk RNA-seq. We thank David Ibberson for help with sequencing the ATAC-seq and Capture-C libraries. This work was supported by the Helmholtz Alliance "Aging and Metabolic Programming, AMPro" (M.C.F. and M.B.). Work in the laboratory of D.T.O. was supported, in part, by an ERC-Advanced Grant ("CTCFStableGenome") from the European Research Council (ERC). Work in the laboratory of M.B. and O.S. was supported, in part, by an ERC-Synergy Grant ("DECODE") from the European Research Council (ERC).

## AUTHOR CONTRIBUTIONS

Conceptualization, M.C.F. and M.B.; investigation, M.C.F., F.H., D.V., Z.A., E.T., S.D.P., Y.T., J.H., D.H., S.M., and A.F.; formal analysis, F.H., J.G.G., E.V., D.V., S.M., A.F., and M.C.F.; visualization, M.C.F. and E.V.; writing – original draft, M.C.F.; writing – review & editing, M.C.F. and M.B.; funding acquisition, M.B.; supervision, M.C.F., O.S., D.T.O., A.F., S.H., M.H., and M.B. All authors edited and agreed on the manuscript.

## DECLARATION OF INTERESTS

The authors declare no competing interests.

## INCLUSION AND DIVERSITY

We support inclusive, diverse, and equitable conduct of research.

Received: August 16, 2022
Revised: May 3, 2023
Accepted: November 13, 2023
Published: December 18, 2023

## REFERENCES

1. SanMiguel, J.M., Young, K., and Trowbridge, J.J. (2020). Hand in hand: intrinsic and extrinsic drivers of aging and clonal hematopoiesis. Exp. Hematol. *91*, 1–9.
2. Tyrrell, D.J., and Goldstein, D.R. (2021). Ageing and atherosclerosis: vascular intrinsic and extrinsic factors and potential role of IL-6. Nat. Rev. Cardiol. *18*, 58–68.
3. Funk, M.C., Zhou, J., and Boutros, M. (2020). Ageing, metabolism and the intestine. EMBO Rep. *21*, e50047.
4. Pentinmikko, N., and Katajisto, P. (2020). The role of stem cell niche in intestinal aging. Mech. Ageing Dev. *191*, 111330.
5. Zheng, D., Liwinski, T., and Elinav, E. (2020). Interaction between microbiota and immunity in health and disease. Cell Res. *30*, 492–506.
6. Barker, N., van Es, J.H., Kuipers, J., Kujala, P., van den Born, M., Cozijnsen, M., Haegebarth, A., Korving, J., Begthel, H., Peters, P.J., et al. (2007). Identification of stem cells in small intestine and colon by marker gene Lgr5. Nature *449*, 1003–1007.
7. Beumer, J., and Clevers, H. (2021). Cell fate specification and differentiation in the adult mammalian intestine. Nat. Rev. Mol. Cell Biol. *22*, 39–53.
8. Ayabe, T., Ashida, T., Kohgo, Y., and Kono, T. (2004). The role of Paneth cells and their antimicrobial peptides in innate host defense. Trends Microbiol. *12*, 394–398.
9. Bajic, D., Niemann, A., Hillmer, A.K., Mejias-Luque, R., Bluemel, S., Docampo, M., Funk, M.C., Tonin, E., Boutros, M., Schnabl, B., et al. (2020). Gut microbiota-derived propionate regulates the expression of Reg3 mucosal lectins and ameliorates experimental colitis in mice. J. Crohns Colitis *14*, 1462–1472.
10. Biton, M., Haber, A.L., Rogel, N., Burgin, G., Beyaz, S., Schnell, A., Ashenberg, O., Su, C.W., Smillie, C., Shekhar, K., et al. (2018). T helper cell cytokines modulate intestinal stem cell renewal and differentiation. Cell *175*, 1307–1320.e22.
11. Garrett, W.S., Gordon, J.I., and Glimcher, L.H. (2010). Homeostasis and inflammation in the intestine. Cell *140*, 859–870.
12. Mihaylova, M.M., Cheng, C.W., Cao, A.Q., Tripathi, S., Mana, M.D., Bauer-Rowe, K.E., Abu-Remaileh, M., Clavain, L., Erdemir, A., Lewis, C.A., et al. (2018). Fasting activates fatty acid oxidation to enhance intestinal stem cell function during homeostasis and aging. Cell Stem Cell *22*, 769–778.e4.
13. Nalapareddy, K., Nattamai, K.J., Kumar, R.S., Karns, R., Wikenheiser-Brokamp, K.A., Sampson, L.L., Mahe, M.M., Sundaram, N., Yacyshyn, M.B., Yacyshyn, B., et al. (2017). Canonical Wnt signaling ameliorates aging of intestinal stem cells. Cell Rep. *18*, 2608–2621.
14. Pentinmikko, N., Iqbal, S., Mana, M., Andersson, S., Cognetta, A.B., Suciu, R.M., Roper, J., Luopajärvi, K., Markelin, E., Gopalakrishnan, S., et al. (2019). Notum produced by Paneth cells attenuates regeneration of aged intestinal epithelium. Nature *571*, 398–402.
15. Elderman, M., Sovran, B., Hugenholtz, F., Graversen, K., Huijskes, M., Houtsma, E., Belzer, C., Boekschoten, M., de Vos, P., Dekker, J., et al. (2017). The effect of age on the intestinal mucus thickness, microbiota

composition and immunity in relation to sex in mice. PLOS One *12*, e0184274.

16. Sovran, B., Hugenholtz, F., Elderman, M., Van Beek, A.A., Graversen, K., Huijskes, M., Boekschoten, M.V., Savelkoul, H.F.J., De Vos, P., Dekker, J., et al. (2019). Age-associated impairment of the mucus barrier function is associated with profound changes in microbiota and immunity. Sci. Rep. *9*, 1437.
17. Gebert, N., Cheng, C.W., Kirkpatrick, J.M., Di Fraia, D., Yun, J., Schädel, P., Pace, S., Garside, G.B., Werz, O., Rudolph, K.L., et al. (2020). Region-specific proteome changes of the intestinal epithelium during aging and dietary restriction. Cell Rep. *31*, 107565.
18. Franceschi, C., Bonafè, M., Valensin, S., Olivieri, F., De Luca, M., Ottaviani, E., and De Benedictis, G. (2000). Inflamm-aging: an evolutionary perspective on immunosenescence. Ann. N. Y. Acad. Sci. *908*, 244–254.
19. Franceschi, C., and Campisi, J. (2014). Chronic inflammation (inflammaging) and its potential contribution to age-associated diseases. J. Gerontol. A Biol. Sci. Med. Sci. *69*, S4–S9. Supplement 1.
20. Ayabe, T., Satchell, D.P., Wilson, C.L., Parks, W.C., Selsted, M.E., and Ouellette, A.J. (2000). Secretion of microbicidal alpha-defensins by intestinal Paneth cells in response to bacteria. Nat. Immunol. *1*, 113–118.
21. He, D., Wu, H., Xiang, J., Ruan, X., Peng, P., Ruan, Y., Chen, Y.G., Wang, Y., Yu, Q., Zhang, H., et al. (2020). Gut stem cell aging is driven by mTORC1 via a p38 MAPK-p53 pathway. Nat. Commun. *11*, 37.
22. Kim, B.H., Chee, J.D., Bradfield, C.J., Park, E.S., Kumar, P., and MacMicking, J.D. (2016). Interferon-induced guanylate-binding proteins in inflammasome activation and host defense. Nat. Immunol. *17*, 481–489.
23. Haber, A.L., Biton, M., Rogel, N., Herbst, R.H., Shekhar, K., Smillie, C., Burgin, G., Delorey, T.M., Howitt, M.R., Katz, Y., et al. (2017). A single-cell survey of the small intestinal epithelium. Nature *551*, 333–339.
24. Roche, P.A., and Furuta, K. (2015). The ins and outs of MHC class II-mediated antigen processing and presentation. Nat. Rev. Immunol. *15*, 203–216.
25. Cheroutre, H., Lambolez, F., and Mucida, D. (2011). The light and dark sides of intestinal intraepithelial lymphocytes. Nat. Rev. Immunol. *11*, 445–456.
26. Giladi, A., Cohen, M., Medaglia, C., Baran, Y., Li, B., Zada, M., Bost, P., Blecher-Gonen, R., Salame, T.M., Mayer, J.U., et al. (2020). Dissecting cellular crosstalk by sequencing physically interacting cells. Nat. Biotechnol. *38*, 629–637.
27. Waldman, A.D., Fritz, J.M., and Lenardo, M.J. (2020). A guide to cancer immunotherapy: from T cell basic science to clinical practice. Nat. Rev. Immunol. *20*, 651–668.
28. Smigiel, K.S., Srivastava, S., Stolley, J.M., and Campbell, D.J. (2014). Regulatory T-cell homeostasis: steady-state maintenance and modulation during inflammation. Immunol. Rev. *259*, 40–59.
29. Sato, T., Vries, R.G., Snippert, H.J., van de Wetering, M., Barker, N., Stange, D.E., van Es, J.H., Abo, A., Kujala, P., Peters, P.J., et al. (2009). Single Lgr5 stem cells build crypt-villus structures in vitro without a mesenchymal niche. Nature *459*, 262–265.
30. Durbin, J.E., Hackenmiller, R., Simon, M.C., and Levy, D.E. (1996). Targeted disruption of the mouse Stat1 gene results in compromised innate immunity to viral disease. Cell *84*, 443–450.
31. Ramana, C.V., Gil, M.P., Schreiber, R.D., and Stark, G.R. (2002). Stat1-dependent and -independent pathways in IFN-γ-dependent signaling. Trends Immunol. *23*, 96–101.
32. Beaurivage, C., Kanapeckaite, A., Loomans, C., Erdmann, K.S., Stallen, J., and Janssen, R.A.J. (2020). Development of a human primary gut-on-a-chip to model inflammatory processes. Sci. Rep. *10*, 21475.
33. Nan, J., Du, Y., Chen, X., Bai, Q., Wang, Y., Zhang, X., Zhu, N., Zhang, J., Hou, J., Wang, Q., et al. (2014). TPCA-1 is a direct dual inhibitor of STAT3 and NF-κB and regresses mutant EGFR-associated human non-small cell lung cancers. Mol. Cancer Ther. *13*, 617–629.
34. Acosta, J.C., Banito, A., Wuestefeld, T., Georgilis, A., Janich, P., Morton, J.P., Athineos, D., Kang, T.W., Lasitschka, F., Andrulis, M., et al. (2013). A complex secretory program orchestrated by the inflammasome controls paracrine senescence. Nat. Cell Biol. *15*, 978–990.
35. Benayoun, B.A., Pollina, E.A., Singh, P.P., Mahmoudi, S., Harel, I., Casey, K.M., Dulken, B.W., Kundaje, A., and Brunet, A. (2019). Remodeling of epigenome and transcriptome landscapes with aging in mice reveals widespread induction of inflammatory responses. Genome Res. *29*, 697–709.
36. Buenrostro, J.D., Wu, B., Chang, H.Y., and Greenleaf, W.J. (2015). ATAC-seq: A method for assaying chromatin accessibility genome-wide. Curr. Protoc. Mol. Biol. *109*, 21.29.1–21.29.9.
37. Sheffield, N.C., and Bock, C. (2016). LOLA: enrichment analysis for genomic region sets and regulatory elements in R and Bioconductor. Bioinformatics *32*, 587–589.
38. Oudelaar, A.M., Downes, D.J., Davies, J.O.J., and Hughes, J.R. (2017). Low-input capture-C: A chromosome conformation capture assay to analyze chromatin architecture in small numbers of cells. Bio Protoc. *7*, e2645.
39. Krausgruber, T., Fortelny, N., Fife-Gernedl, V., Senekowitsch, M., Schuster, L.C., Lercher, A., Nemc, A., Schmidl, C., Rendeiro, A.F., Bergthaler, A., et al. (2020). Structural cells are key regulators of organ-specific immune responses. Nature *583*, 296–302.
40. Larsen, S.B., Cowley, C.J., Sajjath, S.M., Barrows, D., Yang, Y., Carroll, T.S., and Fuchs, E. (2021). Establishment, maintenance, and recall of inflammatory memory. Cell Stem Cell *28*, 1758–1774.e8.
41. Kaiko, G.E., Ryu, S.H., Koues, O.I., Collins, P.L., Solnica-Krezel, L., Pearce, E.J., Pearce, E.L., Oltz, E.M., and Stappenbeck, T.S. (2016). The colonic crypt protects stem cells from microbiota-derived metabolites. Cell *165*, 1708–1720.
42. Shenoy, A.T., Lyon De Ana, C., Arafa, E.I., Salwig, I., Barker, K.A., Korkmaz, F.T., Ramanujan, A., Etesami, N.S., Soucy, A.M., Martin, I.M.C., et al. (2021). Antigen presentation by lung epithelial cells directs CD4+ TRM cell function and regulates barrier immunity. Nat. Commun. *12*, 5834.
43. Beyaz, S., Chung, C., Mou, H., Bauer-Rowe, K.E., Xifaras, M.E., Ergin, I., Dohnalova, L., Biton, M., Shekhar, K., Eskiocak, O., et al. (2021). Dietary suppression of MHC class II expression in intestinal epithelial cells enhances intestinal tumorigenesis. Cell Stem Cell *28*, 1922–1935.e5.
44. Rasa, S.M.M., Annunziata, F., Krepelova, A., Nunna, S., Omrani, O., Gebert, N., Adam, L., Käppel, S., Höhn, S., Donati, G., et al. (2022). Inflammaging is driven by upregulation of innate immune receptors and systemic interferon signaling and is ameliorated by dietary restriction. Cell Rep. *39*, 111017.
45. Naik, S., Larsen, S.B., Gomez, N.C., Alaverdyan, K., Sendoel, A., Yuan, S., Polak, L., Kulukian, A., Chai, S., and Fuchs, E. (2017). Inflammatory memory sensitizes skin epithelial stem cells to tissue damage. Nature *550*, 475–480.
46. Santoro, A., Zhao, J., Wu, L., Carru, C., Biagi, E., and Franceschi, C. (2020). Microbiomes other than the gut: inflammaging and age-related diseases. Semin. Immunopathol. *42*, 589–605.
47. Dobin, A., Davis, C.A., Schlesinger, F., Drenkow, J., Zaleski, C., Jha, S., Batut, P., Chaisson, M., and Gingeras, T.R. (2013). STAR: ultrafast universal RNA-seq aligner. Bioinformatics *29*, 15–21.
48. Ewels, P.A., Peltzer, A., Fillinger, S., Patel, H., Alneberg, J., Wilm, A., Garcia, M.U., Di Tommaso, P., and Nahnsen, S. (2020). The nf-core framework for community-curated bioinformatics pipelines. Nat. Biotechnol. *38*, 276–278.
49. Love, M.I., Huber, W., and Anders, S. (2014). Moderated estimation of fold change and dispersion for RNA-seq data with DESeq2. Genome Biol. *15*, 550.
50. Korotkevich, G., Sukhov, V., Budin, N., Shpak, B., Artyomov, M.N., and Sergushichev, A. (2021). Fast Gene Set Enrichment Analysis.
51. Liberzon, A., Birger, C., Thorvaldsdóttir, H., Ghandi, M., Mesirov, J.P., and Tamayo, P. (2015). The Molecular Signatures Database (MSigDB) hallmark gene set collection. Cell Syst. *1*, 417–425.

52. Zheng, G.X.Y., Terry, J.M., Belgrader, P., Ryvkin, P., Bent, Z.W., Wilson, R., Ziraldo, S.B., Wheeler, T.D., McDermott, G.P., Zhu, J., et al. (2017). Massively parallel digital transcriptional profiling of single cells. Nat. Commun. *8*, 14049.

53. Stuart, T., Butler, A., Hoffman, P., Hafemeister, C., Papalexi, E., Mauck, W.M., Hao, Y., Stoeckius, M., Smibert, P., and Satija, R. (2019). Comprehensive integration of single-cell data. Cell *177*, 1888–1902.e21.

54. Subramanian, A., Tamayo, P., Mootha, V.K., Mukherjee, S., Ebert, B.L., Gillette, M.A., Paulovich, A., Pomeroy, S.L., Golub, T.R., Lander, E.S., et al. (2005). Gene set enrichment analysis: A knowledge-based approach for interpreting genome-wide expression profiles. Proc. Natl. Acad. Sci. USA *102*, 15545–15550.

55. Tirosh, I., Izar, B., Prakadan, S.M., Wadsworth, M.H., Treacy, D., Trombetta, J.J., Rotem, A., Rodman, C., Lian, C., Murphy, G., et al. (2016). Dissecting the multicellular ecosystem of metastatic melanoma by single-cell RNA-seq. Science *352*, 189–196.

56. Hao, Y., Hao, S., Andersen-Nissen, E., Mauck, W.M., 3rd, Zheng, S., Butler, A., Lee, M.J., Wilk, A.J., Darby, C., Zager, M., et al. (2021). Integrated analysis of multimodal single-cell data. Cell *184*, 3573–3587.e29.

57. Ashhurst, T.M., Marsh-Wakefield, F., Putri, G.H., Spiteri, A.G., Shinko, D., Read, M.N., Smith, A.L., and King, N.J.C. (2022). Integration, exploration, and analysis of high-dimensional single-cell cytometry data using Spectre. Cytometry A *101*, 237–253.

58. Van Gassen, S., Callebaut, B., Van Helden, M.J., Lambrecht, B.N., Demeester, P., Dhaene, T., and Saeys, Y. (2015). FlowSOM: using self-organizing maps for visualization and interpretation of cytometry data. Cytometry A *87*, 636–645.

59. McInnes, L., Healy, J., Saul, N., and Großberger, L. (2018). UMAP: uniform manifold approximation and projection. J. Open Source Software *3*, 861.

60. Gontarz, P., Fu, S., Xing, X., Liu, S., Miao, B., Bazylianska, V., Sharma, A., Madden, P., Cates, K., Yoo, A., et al. (2020). Comparison of differential accessibility analysis strategies for ATAC-seq data. Sci. Rep. *10*, 10150.

61. Robinson, M.D., McCarthy, D.J., and Smyth, G.K. (2010). edgeR: a Bioconductor package for differential expression analysis of digital gene expression data. Bioinformatics *26*, 139–140.

62. Yu, G., Wang, L.G., and He, Q.Y. (2015). ChIPseeker: an R/Bioconductor package for ChIP peak annotation, comparison and visualization. Bioinformatics *31*, 2382–2383.

63. Hahne, F., and Ivanek, R. (2016). Visualizing genomic data using Gviz and bioconductor. Methods Mol. Biol. *1418*, 335–351.

64. Lawrence, M., Huber, W., Pagès, H., Aboyoun, P., Carlson, M., Gentleman, R., Morgan, M.T., and Carey, V.J. (2013). Software for computing and annotating genomic ranges. PLOS Comput. Biol. *9*, e1003118.

65. Machlab, D., Burger, L., Soneson, C., Rijli, F.M., Schübeler, D., and Stadler, M.B. (2022). monaLisa: an R/Bioconductor package for identifying regulatory motifs. Bioinformatics *38*, 2624–2625.

66. Downes, D.J., Smith, A.L., Karpinska, M.A., Velychko, T., Rue-Albrecht, K., Sims, D., Milne, T.A., Davies, J.O.J., Oudelaar, A.M., and Hughes, J.R. (2022). Capture-C: a modular and flexible approach for high-resolution chromosome conformation capture. Nat. Protoc. *17*, 445–475.

67. Wingett, S., Ewels, P., Furlan-Magaril, M., Nagano, T., Schoenfelder, S., Fraser, P., and Andrews, S. (2015). HiCUP: pipeline for mapping and processing Hi-C data. F1000Res *4*, 1310.

68. Langmead, B., and Salzberg, S.L. (2012). Fast gapped-read alignment with Bowtie 2. Nat. Methods *9*, 357–359.

69. Cairns, J., Freire-Pritchett, P., Wingett, S.W., Várnai, C., Dimond, A., Plagnol, V., Zerbino, D., Schoenfelder, S., Javierre, B.M., Osborne, C., et al. (2016). CHiCAGO: robust detection of DNA looping interactions in Capture Hi-C data. Genome Biol. *17*, 127.

70. Dabitao, D., Margolick, J.B., Lopez, J., and Bream, J.H. (2011). Multiplex measurement of proinflammatory cytokines in human serum: comparison of the Meso Scale Discovery electrochemiluminescence assay and the Cytometric Bead Array. J. Immunol. Methods *372*, 71–77.

71. Bankhead, P., Loughrey, M.B., Fernández, J.A., Dombrowski, Y., McArt, D.G., Dunne, P.D., McQuaid, S., Gray, R.T., Murray, L.J., Coleman, H.G., et al. (2017). QuPath: open source software for digital pathology image analysis. Sci. Rep. *7*, 16878.

72. Schindelin, J., Arganda-Carreras, I., Frise, E., Kaynig, V., Longair, M., Pietzsch, T., Preibisch, S., Rueden, C., Saalfeld, S., Schmid, B., et al. (2012). Fiji: an open-source platform for biological-image analysis. Nat. Methods *9*, 676–682.

## STAR★METHODS

### KEY RESOURCES TABLE

| REAGENT or RESOURCE | SOURCE | IDENTIFIER |
|---|---|---|
| Antibodies | | |
| Anti-mouse CD4 | Thermo Fisher Scientific | RRID:AB_2865431 |
| Anti-mouse CD8a | Thermo Fisher Scientific | RRID:AB_2572861 |
| Anti-mouse FOXP3 | Cell Signaling Technology | RRID:AB_2747370 |
| Anti-mouse PD-1 | R and D Systems | RRID:AB_354541 |
| Anti-mouse MHC Class II | Novus | RRID:AB_10006678 |
| Anti-rat HRP | Jackson ImmunoResearch | RRID:AB_233980 |
| Anti-goat HRP | Agilent | RRID:AB_2617143 |
| Anti-rabbit HRP | Leica Biosystems | RRID:AB_2891238 |
| Anti-mouse CD4 PE | Thermo Fisher Scientific | RRID:AB_465506 |
| Anti-GFP | Abcam | RRID:AB_300798 |
| Anti-chicken 488 | Thermo Fisher Scientific | RRID:AB_2534096 |
| Anti-mouse CD45 BUV395 | BD Biosciences | RRID:AB_2651134 |
| Anti-mouse CD11b BUV805 | BD Biosciences | RRID:AB_2871246 |
| Anti-mouse CD11c BV711 | BioLegend | RRID:AB_2563905 |
| Anti-mouse CD274 BV421 | BioLegend | RRID:AB_10897097 |
| Anti-mouse CD279 PE-Dazzle | BioLegend | RRID:AB_2566547 |
| Anti-mouse CD324 APC-Fire750 | BioLegend | RRID:AB_2750301 |
| Anti-mouse CD326 APC | Thermo Fisher Scientific | RRID:AB_2716944 |
| Anti-mouse CD4 BUV496 | BD Biosciences | RRID:AB_2813886 |
| Anti-mouse CD44 Alexa Fluor 700 | Thermo Fisher Scientific | RRID:AB_494011 |
| Anti-mouse CD45R/B220 BUV661 | BD Biosciences | RRID:AB_2870244 |
| Anti-mouse CD8 PE-Cy5 | Thermo Fisher Scientific | RRID:AB_468706 |
| Anti-mouse F4/80 Pacific Blue | Thermo Fisher Scientific | RRID:AB_10373419 |
| Anti-mouse Ly6C PerCP-Cy5.5 | BioLegend | RRID:AB_1659242 |
| Anti-mouse Ly6G BV605 | BioLegend | RRID:AB_2565880 |
| Anti-mouse MHC Class II (I-A/I-E) | Thermo Fisher Scientific | RRID:AB_465927 |
| Anti-mouse NK1.1 BV785 | BioLegend | RRID:AB_2564304 |
| Anti-mouse TCR beta chain BV650 | BioLegend | RRID:AB_2810348 |
| Anti-mouse TCR gamma/delta PE-Cy7 | BioLegend | RRID:AB_11203530 |
| Anti-mouse CD326 BV421 | BD Biosciences | RRID:AB_2738073 |
| Anti-mouse CD4 PE | Thermo Fisher Scientific | RRID:AB_465506 |
| Anti-mouse TCR beta APC | Thermo Fisher Scientific | RRID:AB_469480 |
| Anti-mouse CD45 APC | Thermo Fisher Scientific | RRID:AB_469392 |
| Anti-mouse CD326 PE | Thermo Fisher Scientific | RRID:AB_953619 |
| Chemicals, peptides, and recombinant proteins | | |
| AMPure XP beads | Beckman Coulter | A63881 |
| T4 DNA Ligase, HC | Thermo Fisher Scientific | EL0013 |
| TPCA-1 | Sigma-Aldrich | T1452 |
| Recombinant Murine IFN-γ | PeproTech | 315-05 |
| Recombinant Murine IFN-γ (carrier-free) | BioLegends | 575302 |
| Critical commercial assays | | |
| TruSeq Stranded mRNA Library Prep Kit | Illumina | 20020594 |
| HiSeq 3000/4000 SBS Kit (50 cycles) | Illumina | FC-410-1001 |

(*Continued on next page*)

*Continued*

| REAGENT or RESOURCE | SOURCE | IDENTIFIER |
|---|---|---|
| Chromium Next GEM Single Cell 3' Kit v3.1, 16 rxns | 10x Genomics | PN-1000268 |
| NovaSeq 6000 S1 Reagent Kit v1.5 (100 cycles) | Illumina | 20028319 |
| Illumina Tagment DNA TDE1 Enzyme and Buffer Kit | Illumina | 20034210 |
| NextSeq 500/550 High Output Kit v2.5 | Illumina | 20024907 |
| KAPA HyperCapture Reagent Kit | Roche | 9075828001 |
| KAPA HyperCapture Bead Kit | Roche | 9075798001 |
| NEBNext Ultra II DNA Library Prep Kit for Illumina | New England BioLabs | E7645L |
| NEBNext Multiplex Oligos for Illumina Primer sets 1 | New England BioLabs | E7335S/L |
| NEBNext Multiplex Oligos for Illumina Primer sets 2 | New England BioLabs | E7500S/L |
| QuantiTect reverse transcription kit | Qiagen | 205311 |
| Maxima SYBR Green/ROX qPCR Master Mix | Life Technologies | K0221 |
| U-PLEX Custom Biomarker Group 1 (mouse) Assay | Meso Scale Discovery | K15069M |
| BOND Polymer Refine Detection Kit | Leica Biosystems | DS9800 |
| Deposited data | | |
| Sequencing reads (FASTQ) | GEO | GEO:GSE190286 |
| Fluorescence signal data Spectral Flow Cytometry experiment (csv files) | FigShare | [https://doi.org/10.6084/m9.figshare.24271828] |
| Experimental models: Cell lines | | |
| Mouse small intestinal organoid lines | This paper | N/A |
| Experimental models: Organisms/strains | | |
| C57BL/6JRj | Janvier Labs | RRID:MGI:2670020 |
| Lgr5-EGFP-IRES-creERT2 | Jackson | RRID:IMSR_JAX:008875 |
| B6.129S(Cg)-Stat1tm1Dlv/J | Durbin et al.[30] | RRID:IMSR_JAX:012606 |
| Oligonucleotides | | |
| Primer sequences for quantitative real-time PCR, see Table S3 | This paper | N/A |
| Sequences of Capture-C probes, see Table S4 | This paper | N/A |
| Software and algorithms | | |
| Affinity Designer 1 | Affinity Software | https://affinity.serif.com/de/designer/ |
| Amnis IDEAS software v6.03.23 | Amnis (now Cytek) | https://cytekbio.com/pages/imagestream |
| Amnis Inspire acquisition software v201.1.0.744 | Amnis (now Cytek) | https://cytekbio.com/pages/imagestream |
| FlowJo v10 | BD | https://www.flowjo.com/solutions/flowjo |
| SpectroFlo software | Cytek | https://cytekbio.com/pages/spectro-flo |
| GraphPad Prism v9 | GraphPad Software | https://www.graphpad.com/features |
| Fiji | Schindelin et al.[72] | https://fiji.sc |
| QuPath 0.2.3 | Bankhead et al.[71] | https://qupath.github.io |
| Custom R-code | https://github.com/boutroslab/Supp_Funk_2021 | https://doi.org/10.5281/zenodo.8414654 |

## RESOURCE AVAILABILITY

### Lead contact

Further information and requests for resources and reagents should be directed to and will be fulfilled by the Lead contact, Michael Boutros (m.boutros@dkfz.de).

### Materials availability

This study did not generate new materials or unique reagents.

### Data and code availability

Sequencing (Fastq) data have been deposited at Gene Expression Omnibus (GEO) and are publicly available as of the date of publication. Accession numbers are listed in the key resources table.

All original code has been deposited at GitHub (https://github.com/boutroslab/Supp_Funk_2021) and Zenodo. DOIs are listed in the key resources table.
Any additional information required to reanalyze the data reported in this paper is available from the Lead contact upon request.

## EXPERIMENTAL MODEL AND STUDY PARTICIPANT DETAILS

### Mouse husbandry

In this study, male mice of the strain C57BL/6JRj, Lgr5-EGFP-IRES-creERT2 (RRID:IMSR_JAX:008875) (referred to as Lgr5-EGFP reporter mice) and STAT1$^{-/-}$[30] (referred to as STAT1 KO, kind gift by Marieke Essers, DKFZ) were used and genotyped using primers listed in STAR Methods Key resource table. Young (2-3 months of age) and aged (20-22 months of age) mice were bought from Janvier Laboratories (C57BL/6JRj), where mice are maintained under specific-pathogen-free conditions and housed in a controlled environment and health status. Animals are kept at a day/night cycle of 12h/12h, cages are equipped with enrichment and mice are fed with a standard diet of 21% protein ad libitum. Lgr5-EGFP-IRES-creERT2 and STAT1$^{-/-}$ were maintained under the same conditions in the DKFZ animal facility. Animals were sacrificed for organ removal and used for scientific purposes in accordance with Section 4 TierSchG; and according to institutional licenses (DKFZ223, DKFZ223-22, and DKFZ355) in compliance with German federal and state regulations.

### Small intestinal organoid generation, maintenance & treatments

Small intestinal organoids were generated as described before.[29] Proximal small intestine was isolated, cleaned and villi were removed gently with a coverslip. The intestine was cut into small pieces and applied to serial washing steps in pre-chilled PBS and Penicillin-Streptomycin (100U) (15140122, Life Technologies). For crypt isolation the intestinal tissue pieces were transferred into 10 ml of Gentle Cell Dissociation Reagent (07174, STEMCELL Technologies) and incubated for 15 mins at room temperature (RT). After incubation, the tube was shaken vigorously for approximately to release the crypts and the solution was passed through a 70 μm cell strainer (43-10070-40, pluriSelect) into 30 ml PBS (20012027, Gibco) to stop the enzymatic digest and to exclude larger tissue pieces. Crypts were resuspended in Matrigel (Growth Factor Reduced, 356231, Corning) to obtain a final crypt concentration of 10 000 crypts per ml, which corresponds to 200 crypts per well of a 48-well plate. 20 μl of Matrigel-Crypt-Mix per well were seeded in a 48-well plate and 250 μl of IntestiCult Organoid Growth Medium (06005; STEMCELL Technologies) with Primocin (1:500, always added fresh) (ant-pm-05, InvivoGen) were added to each well and incubate at 37°C, in a humidified $CO_2$ incubator. Medium was renewed every 2-3 days and organoids were split every 7 days. For TPCA-1 treatment, organoids were treated with 5μM TPCA-1 (T1452, Sigma Aldrich) and controls with DMSO at the same final concentration for 24 hrs. For IFNγ treatment, organoids were treated with 2ng/ml IFNγ (575302, BioLegend Europe) or 500pg/ml IFNγ (315-05, PeproTech) and controls with PBS for three, six or 24 hrs.

## METHODS DETAILS

### Single-cell dissociation of small intestinal tissue and FACS sorting of epithelial cells

Proximal small intestinal tissue was isolated, cleaned and incubated for 5 min in ice-cold PBS with 10 mM EDTA (AM9261, Invitrogen), followed by gentle shaking for 1 minute (min). Tissue was transferred into a new PBS solution with 10 mM EDTA and 10 μM Y-27632 (Dihydrochloride Rock inhibitor, SEL-S1049, Biozol Diagnostica), and incubated for 30 mins at 4 °C; released epithelial cells were filtered through a 70 μm cell strainer (43-10070-40, pluriSelect). To obtain a single cell suspension of epithelial cells, cells were resuspended in Advanced DMEM/F12 (AD) (11540446, Gibco) supplemented with TrypLE (12604-013, Gibco) and DNase I (0.3 U/mL (07900, STEMCELL Technologies)) and incubated 45 mins at 37 °C and further filtered through a 20 μm cell strainer (43-10020-40, pluriSelect). Cells were centrifuged and resuspended in 600 μl Blocking buffer (PBS + 2 % BSA (B9000S, New England Biolabs)) and incubated for 5 min on ice. Cells were stained with anti-CD326 (EpCam)-PE conjugated (12-5791-81; Invitrogen) and anti-CD45-APC conjugated (17-04510-82; eBioscience), both diluted 1:300 directly into the blocking buffer and incubated for 15 min on ice. Living cells were gated by DAPI dye exclusion, epithelial cells were isolated as EpCAM$^+$, CD45$^-$ cells and first 25 000 cells were sorted for single-cell RNA-Sequencing, and then 300 000 cells per sample for bulk RNA-Seq, into IntestiCult Organoid Growth Medium (06005; STEMCELL Technologies). Sorting was performed on a BD FACS Aria I cell sorter (100 μm nozzle size).

For bulk RNA-Seq, the cells were resuspended in 300 μl RLT buffer (79216; QIAGEN) with 1:100 ß-Mercaptoethanol (63689; Sigma Aldrich). RNA extraction was conducted via QIAGEN RNeasy Mini kit (74106; Qiagen), including an on-column DNase digestion using the RNase-free DNase Set (79254; Qiagen).

### Bulk RNA-Seq library generation & sequencing

Illumina sequencing libraries were prepared using the TruSeq Stranded mRNA Library Prep Kit (20020594, Illumina) according to the manufacturer's protocol. Briefly, poly(A)+ RNA was purified from 500 ng of total RNA using oligo(dT) beads, fragmented to a median insert length of 155 bp and converted to cDNA. The ds cDNA fragments were then end-repaired, adenylated on the 3′ end, adapter ligated and amplified with 15 cycles of PCR. The libraries were quantified using Qubit ds DNA HS Assay kit (Life Technologies-Invitrogen) and validated on an Agilent 4200 TapeStation System (Agilent technologies). Based on Qubit quantification and sizing

analysis, multiplexed sequencing libraries were normalized, pooled and sequenced on HiSeq 4000 single-read 50 bp with a final concentration of 250 pM (spiked with 1% PhiX control).

### Bulk RNA-Seq analysis of freshly isolated intestinal epithelium (1), intestinal organoids (2)

Raw sequencing reads were aligned using STAR aligner (vSTAR_2.6.1d).[47] To this end, the nf-core pipeline rnaseq (v1.4.2, doi: 10.5281/zenodo.1400710) was employed.[48] A conventional DESeq2 (1.30.1) pipeline was used to perform differential expression analysis.[49] (1) 23,703 or (2) 24,674 transcripts were detected. Variance stabilizing transformation was adopted to stabilize the variance of genes with low read count for visualization of the sample dispersion. Significantly differentially expressed genes were called within a threshold of FDR < 10 % and an absolute $\log_2$ FC > 0.5. Molecular signature and enrichment analysis were performed with the FGSEA package and hallmark signatures from MsigDB.[50,51] Overlap analysis between experiments 1) and 2) was performed using the online Venn diagram tool () by VIB / U Gent, Bioinformatics & Evolutionary Genomics.

### Single-cell RNA-Seq library generation & sequencing

Cells from the proximal small intestine were prepared for FACS sorting and living epithelial cells were gated by DAPI dye exclusion, epithelial cells were isolated as $EpCAM^+$, $CD45^-$ cells. Per samples, 25 000 cells were sorted into IntestiCult Organoid Growth Medium (0600-0, -2 and -3 combined, STEMCELL Technologies), centrifuged and directly processed for library generation with the 10x Genomics technology according to the manufacturer's protocol. Library generation was performed using the Chromium Controller instrument, the Chromium Single Cell 3′ Library, and Gel Bead Kit v3, and the Chromium Single Cell B Chip Kit. All cleanup steps were conducted using AMPure XP beads (A63881, Beckman Coulter). In short, about 20,000 cells from each sample were loaded per lane of the chip. Gel Beads in Emulsion (GEMs) were successfully generated for all samples, reverse transcription of mRNA was followed by cDNA amplification using 11 or 12 PCR cycles. The final library was generated and amplified in a Sample Index PCR using 12 or 13 cycles. All libraries sequenced had an average fragment size of 483 – 515 bp. To minimize technical artifacts, we pooled the final libraries and sequenced the multiplex on 2 lanes of a NovaSeq 6000 instrument with 100 cycle S1 reagent kits (read1 (cell barcode + UMI): 28 bp, read2 (transcript): 94 bp, i7 (sample index): 8 bp).

### Single-cell RNA-Seq analysis

Raw, demultiplexed sequencing data was processed with 'cellranger' v3.0.1[52] with parameters '–transcriptome=mm10-1.2.0' and '–expect-cells=5000'. The filtered count matrices were further processed with Seurat v4.0.5: only cells with more than 10 000 UMI counts and with at most 15% of UMI counts from mitochondrial genes were selected for further analysis (Figure S2A). Cells from different replicates were integrated using Seurat's 'IntegrateData'.[53] For visualization, a tSNE embedding of cells was computed based on the first 10 Principal components of the integrated and scaled data, using a UMAP embedding of the same as initialization. Cells were assigned to their respective types based on the labels transferred from cells of[23] using Seurat's 'TransferData' but refining class labels along the Stem-Enterocyte axis to obtain simpler cell types, less dependent on cell cycle phases. Absolute differences in cell type ratios between young and aged samples was tested for with a paired t-test. Fold changes of cell type proportions were tested for with DEseq2 with size factors based on total counts and a global overdispersion estimate. Original UMI counts from all cells of each gene, sample and - for cell type specific analyses - cell type were aggregated by summation to form pseudo bulk aggregates and differential expression testing was performed on them separately for each cell type using DEseq2, adjusting for Chromium run. PCA embedding of samples was computed using DEseq2's 'varianceStabilizingTransformation' without adjusting for Chromium run. All single-cell RNA-seq analyses and visualizations have been performed in R v4.1.0 making heavy use of R packages 'data.table' and ggplot2.

Fgsea[50] (the fast R-package implementation of the pre-ranked gene set enrichment analysis algorithm (GSEA)[54]) was used to perform the gene set enrichment analysis on each cell type based on a subset of the hallmark gene sets extracted from the Molecular Signature Database (MsigDB) collection. Those are gene sets that can be linked to the ageing process.

A smaller subset of 6 hallmark gene sets (HALLMARK_INTERFERON_ALPHA_RESPONSE, HALLMARK_INTERFERON_GAMMA_RESPONSE, HALLMARK_ALLOGRAFT_REJECTION, HALLMARK_TNFA_SIGNALING_VIA_NFKB, HALLMARK_INFLAMMATORY_RESPONSE, HALLMARK_IL6_JAK_STAT3_SIGNALING) was then combined to create the list of genes related to the inflammaging phenotype. That consisted of a total of 151 unique genes present in the single cell data. To associate an inflammaging score to each cell, later averaged to each cell type, the AddModuleScore function[55] from Seurat V4[56] was used. The inflammaging score was then scaled to range from 0 to 1.

### Spectral flow cytometry

Single cells were isolated from the proximal small intestine of young and aged Lgr5-EGFP mice as described above for FACS sorting. For flow cytometric analyses cells were stained in PBS 2% FCS 0.5 mM EDTA for 25 min with corresponding antibodies (as listed in STAR Methods Key Resource table) and washed once, followed by centrifugation for 5 min at 400g. Finally, cells were filtered through a 35-40μM filter and acquired on a spectral analyzer (Cytek Aurora, Cytek).

### Spectral flow cytometry data analysis

Recorded FCS files were unmixed using SpectroFlow (Cytek) and imported into FlowJo (BD). After gating out debris, doublet events and dead cells, expression data was transformed using the ''logicle'' transform using FlowJo (v.10.7.1). Exported files were loaded

into R and processed using the Spectre package[57] For clustering and dimensionality reduction, FlowSom[58] uniform manifold approximation and projection[59] were used. Epithelial cells and immune cells were identified via EPCAM and CD45 expression, respectively, and further subset for downstream quantification and surface marker expression analysis. $CD45^+$ cells were annotated based on canonical cell type specific surface markers.

For analysis of heterotypic physically interacting cells, we followed a $CD45^+$ $EPCAM^+$ gating strategy from[26] and further analyzed interacting cells for co-expression of CD4, TCRβ and Lgr5, which would identify $Lgr5^+$ ISCs interacting with $TCR\beta^+$ $CD4^+$ T cells. Frequency of such interacting cells was then quantified.

### Image flow cytometry & data analysis

Single cell isolation, preparation and staining as described for Spectral Flow cytometry. Data acquistion occured on a Luminex ImageStream MkII using the Inspire acquisition software (version 201.1.0.744). Cells were imaged using a 40x objective, at a low flow rate and an extended depth of field (EDF) imaging mode. Data analysis was performed with IDEAS software (version 6.03.23).

### Organoid RNA isolation, cDNA generation and quantitative real-time PCR

Organoids from typically 3 wells were harvested in 300 μl Cell Recovery Solution (354253; Gibco) and lysed in 300 μl RLT lysis buffer. Samples were filtered with QIAShredder (79656; Qiagen) columns, followed by RNA isolation with QIAGEN RNeasy Mini kit (74106; Qiagen), including an on-column DNase digestion using the RNase-free DNase Set (79254; Qiagen). cDNA was prepared from 0.5–1 μg total RNA with the QuantiTect reverse transcription kit (205311; Qiagen), according to the manufacturer's protocol. cDNA was diluted to 10 ng/μl and 20 ng were used for each quantitative real-time PCR reaction, using Maxima SYBR Green (K0221; Life Technologies) on the Lightcycler480 (Roche) in a 384-well format. Relative expression of each gene was calculated relative to the housekeeping gene *36B4* as $2^{-\Delta Ct}$. Oligonucleotide sequences are listed in Table S3, all primers were validated prior to use in a cDNA dilution series.

### Organoid single-cell dissociation and ATAC-Seq library generation

Per sample, organoids from 8 wells (48 well-plate) were harvested for single cell dissociation. Matrigel was dissolved using ice-cold Advanced DMEM/F12 (AD) (11540446, Gibco), washed once with AD and then subjected to an enzymatic digest with TrypLE (12604-013, Gibco) + DNase I (07900, STEMCELL Technologies) at a final concentration of 0.1 mg/ml for 5 mins at 37 C. Digestion was stopped by addition of AD + 10% FBS. Cells were washed twice with AD and then passed through a 20 μm cell strainer (43-10020-40, pluriSelect) (pre-equilibrated with AD). ATAC-Seq library generation was based on.[36] Organoids were dissociated to single cells as described before. 100 000 single cells were treated with 50 μl cold lysis buffer (0,1% NP-40 (492016, Millipore), 0,1% Tween-20 (P1379, Sigma Aldrich), 0,01% Digitonin (G9441, Promega) in Resuspension buffer (RB)) for 3 min on ice. Then 1 ml Washing buffer (0,1% Tween-20 in RB) was added to the cells and centrifuged for 10 min at 4C at 500g. Supernatant was discarded and the pellet including the nuclei was resuspended in a 50 μl transposition reaction mix (Illumina Tagment DNA Enzyme and Buffer Kit, 20034210). Transposition reaction and PCR amplification was carried out according to,[36] using Nextera i5 and i7 index adapters to generate double index libraries. Libraries were purified via double-sided bead purification using AMPure XP beads (A63881, Beckman Coulter) and the library quality and quantity were assessed using Agilent High Sensitivity DNA Bioanalysis Chips (5067-4626, Agilent) and QuBit, respectively.

For ATAC-Seq libraries, of freshly isolated intestinal epithelial cells, tissue was dissociated and prepared for FACS-sorting as described below. Per sample, 100.000 epithelial cells ($EpCAM^+$, $CD45^-$) were sorted and then processed as described for organoids samples.

### ATAC-Seq sequencing and analysis

ATAC-Seq libraries of all samples per *ex vivo* and *in vivo* experiment were pooled and sequenced on a NextSeq, Paired-end 75bp, this generated a total of 727 107 568 reads of which 725 802 530 passed quality control for the *ex vivo* experiment, for *in vivo* 733 374 374 reads of which 108 528 869. Raw reads were processed using the end-to-end integrated nf-core pipeline *atacseq* (version 1.2.1, https://doi.org/10.5281/zenodo.2634132,[48]). The results of the *broadPeak* analysis were used to pursue downstream analysis. The analysis was based on the ENSEMBL mouse genome release GRCm38.p6. Given the insights of the comparative analysis from Gontarz and colleagues we analysed our data set accordingly employing R/edgeR to call differentially open chromatin regions.[60,61] As statistic for gene set enrichment analysis, we employed the equation stat= qnorm(1-pvalue/2)*sign(log2FC). Resulting differentially open peaks were annotated using ChipSeeker[62] and the M. musculus mm10 UCSC transcript database (TxDb.Mmusculus.UCSC.mm10.knownGene). For PCA analysis data was variance stabilized using DESeq2. Differentially open peaks were called significant if their Benjamini Hochberg corrected p-value was below 0.1 (10 % FDR). For comparing ATAC-Seq differentially open chromatin regions with differentially expressed transcripts, results were merged by the official gene symbol. The $\log_2$ fold changes were z-scaled and results plotted. A linear regression shows the correlation of the two distributions. In order to understand the transcription factors involved in the regulation of transcripts by open chromatin regions, we employed Locus Overlap Analysis (LOLA) using the LOLACore database and differentially open chromatin regions in genes assigned to the HALLMARK of interferon gamma response.[37,51] Results were visualized using R/Gviz and R/GenomicRanges.[63,64] For motif enrichment analysis the monaLisa R package was used and enrichment of motifs was performed as described in the original publication using species number 10090.[65]

### Capture-C Extraction Protocol

Chromatin was extracted and fixed as described previously,[66] following the protocol for low input and adapting centrifugation steps to organoid cells (400 g). Briefly, 25,000 organoid cells were trypsinized, collected in 1ml medium and crosslinked with 134μl of 16% formaldehyde (1.89% final; ThermoFisher Scientific, #10751395) while rotating for 10 min at room temperature. Cells were quenched with 162μl 1M cold glycine, washed with cold PBS and lysed for 20 minutes at 4°C in 500μl lysis buffer (10mM Tris pH 8, 10mM NaCl, 0.2% NP-40, supplemented with cOmplete proteinase inhibitors (Roche)) prior to snap freezing on dry ice. Fixed chromatin was stored at -80°C.

### Capture-C Library Construction Protocol

Capture-C libraries were prepared as described previously, following the recommendations for Low Input samples.[66] Briefly, lysates were thawed on ice, pelleted and resuspended in 200μl 1x DpnII buffer (New England Biology). The nuclei were subsequently permeabilized with SDS (ThermoFischer Scientific, AM9820, 0.28% final concentration, 1hr, 37°C, interval shaking 500rpm, 30 sec on/off), quenched with Triton X 100 (1.67% final concentration, 1hr, 37°C, interval shaking 500rpm, 30 sec on/off) and digested for 24 hours with 3x10μl DpnII (homemade, 37°C, interval shaking 500rpm, 30 sec on/off). The digested chromatin was then in situ ligated with 8μl T4 Ligase (240U, ThemoFirsher Scientific, EL0013) in a volume of 1440μl (20 hours, 16°C). Following this, the nuclei containing ligated chromatin were pelleted to remove any non-nuclear chromatin, reverse-crosslinked and the ligated DNA was phenol-chloroform purified. The sample was resuspended in 100μl water and sonicated 13x (Bioruptor Pico, 30sec on/off) to obtain fragments of ~200bp, followed by a concentration using AmpureX beads (Beckman Coulter A63881, ratio: 1.8x). All material was adaptor-ligated and indexed in one reaction using the NEBNext Ultra II DNA Library Prep Kit for Illumina (New England Biolabs: E7645L) and NEBNext Multiplex Oligos for Illumina Primer sets 1 (New England Biolabs #E7335S/L) and 2 (New England Biolabs #E7500S/L). The libraries were amplified with 8 PCR cycles using Herculase II Fusion Polymerase kit (Agilent #600677) and their appropriate size assessed via Bioanalyzer. Capture-C probe sequences are listed in Table S4.

Libraries were next hybridized in the following way: For each promoter-containing DpnII restriction fragment we designed one-two capture probes (aligned to mm10, 70bp each) using the online tool designed by the Hughes lab (CapSequm2: https://oligo.readthedocs.io/en/latest/) with the following filtering parameters: Duplicates: <2, Density <30, SRepeatLength <30, Duplication: FALSE. Note that only one capture probe could be designed for the first Ciita TSS (STAR Methods Key Resource Table). The 5' biotinylated probes were pooled at a 2.9 nM each and the samples were multiplexed by mass prior to hybridization (2ug each, according to Qubit dsDNA BR Assay, Invitrogen #Q32850). Hybridization was carried out using the KAPA HyperCapture system (Roche, KAPA HyperCapture Reagent Kit #9075828001, KAPA HyperCapture Bead Kit #9075798001) according to Roche protocol for 72 hours followed by a 24 hours hybridization (double Capture). During the PCR amplification steps libraries were amplified for 18 cycles to ensure all of the low input sample is captured. Captured libraries were quantified by qPCR using the KAPA Sybr Fast Universal kit (KAPA #KK4602) and sequenced on Illumina NextSeq 500.

### Capture-C analysis

Paired-end reads were aligned to mm10 and filtered for Hi-C artefacts using HiCUP[67] and Bowtie 2,[68] with fragment filter set to 100-800 bp. Quality was evaluated by ensuring a high proportion of valid reads (generally high, above 50%, for two IFNγ-treated samples of organoid 77 36.8 and 37.7%, respectively). High restriction digestion efficiency was assessed by evaluating the percentage of re-ligated fragments, suggesting that digestion efficiency was above 70% for all samples (lowest: 73.1%). Read counts of reads aligning to captured gene promoters were then called by CHiCAGO.[69]

For scatterplots we first determined all interactions between promoters and a given set of intervals (i.e. ATAC peaks). To enable a robust analysis of the Low Input data, ATAC peaks were extended for this to cover two adjacent DpnII restriction fragments on each side. Next, for each promoter-interval interaction we quantified the sum of read counts across all DpnII fragments overlapping this interval. This number was then divided by the total number of interval-overlapping DpnII fragments and total read coverage of the interacting promoter to obtain mean normalized read counts.

### Cytokine assay

For the cytokine assay, we used the electrochemiluminescence-based multiplex assay[70] (K15069L-1; MSD U-PLEX Biomarker Group 1 (Mouse) Multiplex Assay; Meso Scale Discovery, Inc.) according to manufacturer's protocol. We measured the medium that had been added to organoid culture for 2 days before measurement. 4 biological replicates per age were measured in technical duplicates.

### Histology, immunohistochemistry, immunofluorescence and quantification

Proximal small intestinal pieces were cleaned and fixed as swiss roll in 4% paraformaldehyde overnight at RT, paraffin embedded and sectioned (2 μm). Immunohistochemistry was performed on a Bond max System (DS9800; Leica Biosystems), using the Bond Polymer Refine Detection Kit (DS9800; Leica Biosystems). Sections were first applied to a peroxide blocking step for epitope retrieval using Epitope Retrieval Solution I and II (AR9640, Leica Biosystems), followed by primary antibody incubation for 30 mins at RT (PD-L1: 1 hr incubation time) and secondary antibody for 20 mins at RT used antibodies are listed in STAR Methods Key Resource Table. DAB enzymatic staining development was performed for 10 mins at 37C, using the Enzyme Pretreatment Kit (AR9551; Leica Biosystems) and followed by a counterstaining with Hematoxylin (AR9551; Leica Biosystems). Slides were scanned with a Leica

Aperio AT2. For quantification the QuPath analysis software[71] was used. In brief, regions for measurement were selected, followed by the positive cell detection command, which counts all cells and all DAB-positive cells, resulting in the percentage of positive cells in the region of interest. Intensity threshold parameters for the positive cell detection command were as follows: Score compartment: Nucleus: DAB OD mean; Threshold: 0.15, 0.2 or 0.3 depending on the analysed staining while thresholds for the same staining were not changed between samples. MHC-II staining was analysed with the Fiji software[72] using the threshold command first to select tissue area and second to detect DAB-positive tissue areas. Statistical significance was tested by an unpaired t-test (two-sided). 3-4 biological replicates per age were stained and quantified.

For immunofluorescence staining, sections were blocked with 5% normal goat serum, anti-GFP antibody was incubated over night at 4C. Anti-chicken-488 and CD4-PE antibodies were incubated on the next day for 2 hrs at RT. Slides were scanned with a ZEISS Axioscan7.

## QUANTIFICATION AND STATISTICAL ANALYSIS

All statistical tests were performed with the GraphPad Prism Software (Version 9.2.0 & 9.5.0) or in the R program. All experiments include at least 3 biological replicates (biological replicate is defined as individual animal or organoid line derived from an individual animal) per age group or per treatment. Statistical details are described in the respective figure legend and exact p-values are plotted within the respective graph.

**Developmental Cell, Volume *58***

## Supplemental information

# Aged intestinal stem cells propagate cell-intrinsic sources of inflammaging in mice

**Maja C. Funk, Jan G. Gleixner, Florian Heigwer, Dominik Vonficht, Erica Valentini, Zeynep Aydin, Elena Tonin, Stefania Del Prete, Sylvia Mahara, Yannick Throm, Jenny Hetzer, Danijela Heide, Oliver Stegle, Duncan T. Odom, Angelika Feldmann, Simon Haas, Mathias Heikenwalder, and Michael Boutros**

# Aged intestinal stem cells propagate cell-intrinsic sources of inflammaging

Maja C. Funk[1], Jan G. Gleixner[1,2,3,4], Florian Heigwer[1,5], Dominik Vonficht[4,6,7], Erica Valentini[1], Zeynep Aydin[1], Elena Tonin[1], Stefania Del Prete[8], Sylvia Mahara[9], Yannick Throm[1], Jenny Hetzer[10], Danijela Heide[10], Oliver Stegle[2,3], Duncan T. Odom[8], Angelika Feldmann[9], Simon Haas[6,7,11,12], Mathias Heikenwalder[10,13] and Michael Boutros[1,14,*]

[1] German Cancer Research Center (DKFZ), Division Signaling and Functional Genomics; Heidelberg University, BioQuant & Department of Cell and Molecular Biology, Medical Faculty Mannheim; Heidelberg University, Institute for Human Genetics, Medical Faculty Heidelberg, 69120 Heidelberg, Germany

[2] German Cancer Research Center (DKFZ), Division of Computational Genomics and Systems Genetics, 69120 Heidelberg, Germany

[3] Genome Biology Unit, European Molecular Biology Laboratory (EMBL), 69117 Heidelberg, Germany

[4] Faculty of Biosciences, Heidelberg University, 69117 Heidelberg, Germany

[5] Department of Life Sciences and Engineering, University of Applied Sciences Bingen, 55411 Bingen am Rhein, Germany

[6] Heidelberg Institute for Stem Cell Technology and Experimental Medicine (HI-STEM gGmbH), 69120 Heidelberg, Germany

[7] German Cancer Research Center (DKFZ), Division of Stem Cells and Cancer, DKFZ-ZMBH Alliance, 69120 Heidelberg, Germany

[8] German Cancer Research Center (DKFZ), Division Regulatory Genomics and Cancer Evolution, 69120 Heidelberg, Germany

[9] German Cancer Research Center (DKFZ), Junior Research Group Mechanisms of Genome Control, 69120 Heidelberg, Germany

[10] German Cancer Research Center (DKFZ), Division Chronic Inflammation and Cancer, 69120 Heidelberg, Germany

[11] Berlin Institute of Health (BIH), Charité Universitätsmedizin Berlin, 10178 Berlin, Germany

[12] Max Delbrück Center for Molecular Medicine in the Helmholtz Association, Berlin Institute for Medical Systems Biology, 10115 Berlin, Germany

[13] The M3 Research Center, Medical Faculty Tübingen, Eberhard Karls University of Tübingen, 72074 Tübingen, Germany

[14] Lead contact

*Corresponding author: m.boutros@dkfz.de

## Supplementary Figures & Tables

**Figure S1.** Bulk RNA-Seq and single-cell RNA-Seq from young and aged proximal small intestinal epithelium.
*Related to Figures 1, 2 and 4.*

**Figure S2.** QC *in vivo* single-cell RNA-Seq of the proximal small intestinal epithelium.
*Related to Figure 2.*

**Figure S3.** The immune microenvironment of the ageing intestine.
*Related to Figure 4.*

**Figure S4.** *Ex vivo* bulk RNA-Seq from young and aged organoids.
*Related to Figure 5.*

**Figure S5.** Secreted factors are not the major source of intrinsic inflammaging in aged intestinal organoids.
*Related to Figures 5 and 6.*

**Figure S6.** Chromatin remodelling accompanies inflammaging in the intestinal epithelium.
*Related to Figure 6.*

**Figure S7**. Age-related changes in chromatin accessibility of intestinal epithelial cells *in vivo*.
*Related to Figure 7.*

**Table S3.** Primers for qRT-PCR and genotyping of Lgr5-EGFP-IRES-creERT2 and Stat1 KO mouse lines.
*Related to STAR Methods Key Resource Table.*

**Table S4.** Capture-C probe sequences.
*Related to STAR Methods Key Resource Table.*

## Figure S1

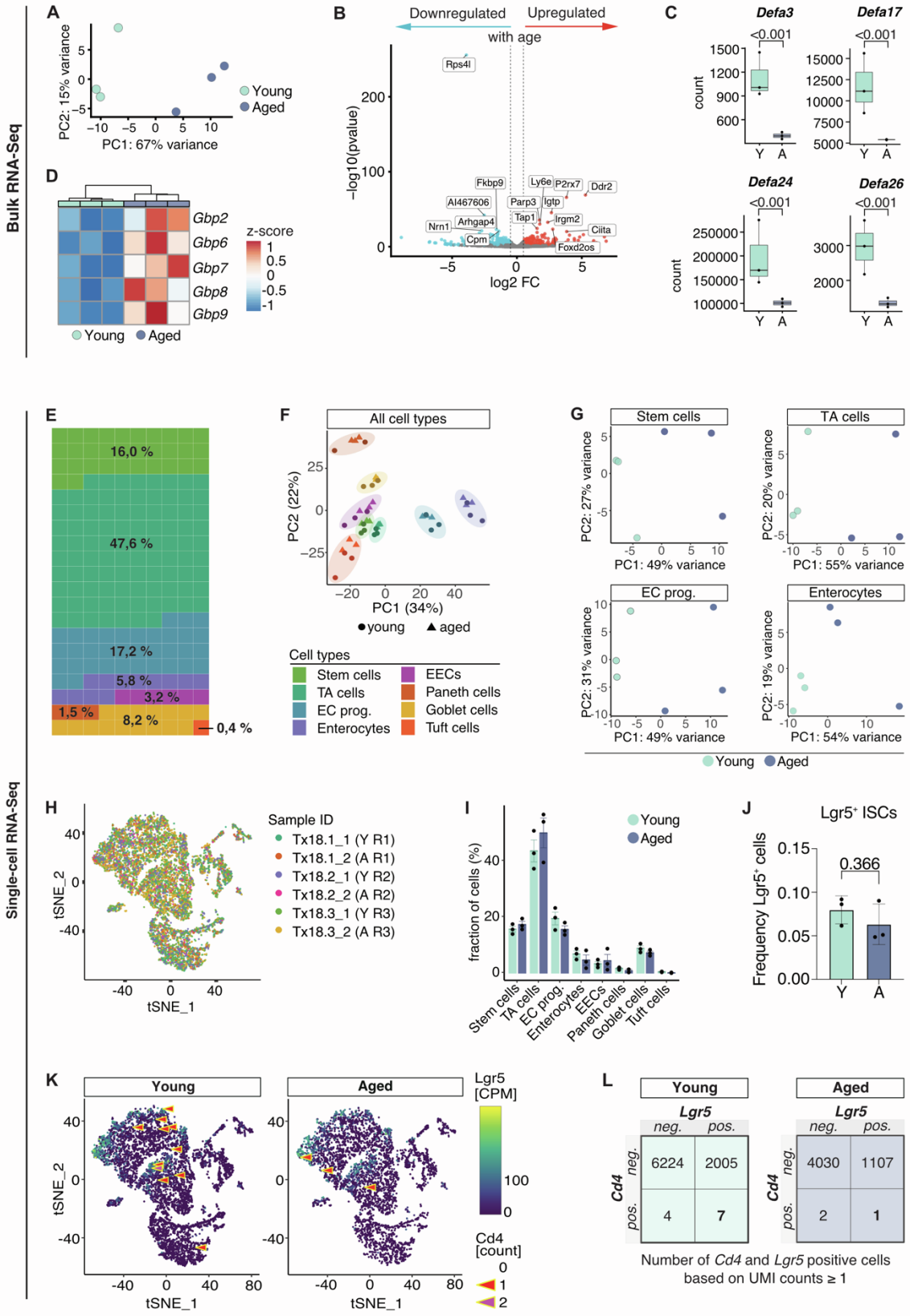
Bulk RNA-Seq
A
PC2: 15% variance
PC1: 67% variance
Young
Aged
B
Downregulated
Upregulated
with age
−log10(pvalue)
log2 FC
Rps4l
Fkbp9
Ly6e
P2rx7
Ddr2
AI467606
Parp3
Igtp
Tap1
Irgm2
Nrn1
Arhgap4
Cpm
Ciita
Foxd2os
C
Defa3
Defa17
Defa24
Defa26
<0.001
count
Y
A
D
Gbp2
Gbp6
Gbp7
Gbp8
Gbp9
z-score
Young
Aged
Single-cell RNA-Seq
E
16,0 %
47,6 %
17,2 %
5,8 %
3,2 %
1,5 %
8,2 %
0,4 %
F
All cell types
PC2 (22%)
PC1 (34%)
young
aged
Cell types
Stem cells
TA cells
EC prog.
Enterocytes
EECs
Paneth cells
Goblet cells
Tuft cells
G
Stem cells
TA cells
EC prog.
Enterocytes
PC2: 27% variance
PC1: 49% variance
PC2: 20% variance
PC1: 55% variance
PC2: 31% variance
PC1: 49% variance
PC2: 19% variance
PC1: 54% variance
Young
Aged
H
Sample ID
Tx18.1_1 (Y R1)
Tx18.1_2 (A R1)
Tx18.2_1 (Y R2)
Tx18.2_2 (A R2)
Tx18.3_1 (Y R3)
Tx18.3_2 (A R3)
tSNE_1
tSNE_2
I
Young
Aged
fraction of cells (%)
Stem cells
TA cells
EC prog.
Enterocytes
EECs
Paneth cells
Goblet cells
Tuft cells
J
Lgr5⁺ ISCs
Frequency Lgr5⁺ cells
0.366
Y
A
K
Young
Aged
Lgr5 [CPM]
Cd4 [count]
tSNE_1
tSNE_2
L
Young
Aged
Lgr5
neg.
pos.
Cd4
6224
2005
4
7
4030
1107
2
1
Number of Cd4 and Lgr5 positive cells
based on UMI counts ≥ 1

**Figure S1. Bulk RNA-Seq and single-cell RNA-Seq from young and aged proximal small intestinal epithelium.**
**Related to Figure 1, 2 and 4.**

**(A)** Age of the mice is the first driving force to separate the samples of the bulk RNA-Seq experiment, as shown by Principal component (PC) analysis on the bulk RNA-Seq samples, obtained from freshly isolated small intestinal epithelial cells of young (n=3) and aged (n=3) mice. PC1 and PC2 are plotted on the x and y axis, variance explained by PC1 and PC2 in %.

**(B)** Volcano plot showing differentially expressed genes upon ageing (aged over young) in the small intestinal epithelium, red: significantly (FDR≤10%) upregulated (log2 fold change (log2FC > 0.5), blue: significantly downregulated (log2FC < 0.5), grey: not significant (FDR>10%), absolute log2FC < 0.5); gene names of the 15 most significantly changed genes upon ageing are plotted.

**(C)** Downregulation of alpha defensins upon ageing. Count plots based on *in vivo* bulk RNA-Seq experiment for *Defa3*, *Defa17*, *Defa24* and *Defa26*. Bars represent the average counts for all young (n=3) and all aged mice (n=3), and dots represent the counts of the individual sample.

**(D)** Upregulation of genes encoding for guanylate-binding proteins (Gbps) upon ageing in the small intestinal epithelium. Relative mean expression as z-score per Gbp gene (row) and sample (column), color code indicates z-score.

**(E)** Cell type proportions across all samples in %, represented in a waffle plot. Each square of the waffle plot represents a 0.5% proportion of all cells.

**(F)** Young and aged samples cluster primarily according to their cell type identity as indicated by a PCA plot for all samples (young and aged) and cell types per sample.

**(G)** PCA plot for all samples per cell type: Stem cells, TA cells, EC prog. and enterocytes.

**(H)** tSNE visualization of all sequenced cells (13 360) and color-coded by the sample they originated from.

**(I)** Average cell fraction (in %) per sample for all young and all aged samples; data points indicate the percentage of individual samples.

**(J)** Frequency of $Lgr5^{+}$ ISCs among all cells from the small intestine measured by FACS from young (n=3) and aged (n=3) Lgr5-EGFP mice.

**(K)** tSNE visualization of all young and aged sequenced cells color-coded by CPM for *Lgr5* expression. Arrowheads highlight cells with a UMI count > 0 for *Cd4*. Red arrowheads indicate cells with a UMI count = 1 for *Cd4*, and Purple arrowheads a UMI count = 2 for *Cd4*.

**(L)** Tables indicating the total numbers of cells that are single-positive, double-negative, or double-positive for *Cd4* and *Lgr5* expression from all sequenced young (left) and aged (right) intestinal epithelial cells. Positive cells are defined by a UMI count ≥ 1 for the respective gene.

log2FC: log2 fold change, PC: principal component, TA: transit-amplifying, EC prog.: enterocyte progenitors, EECs: enteroendocrine cells, CPM: counts per million total UMI counts of a cell.

## Figure S2

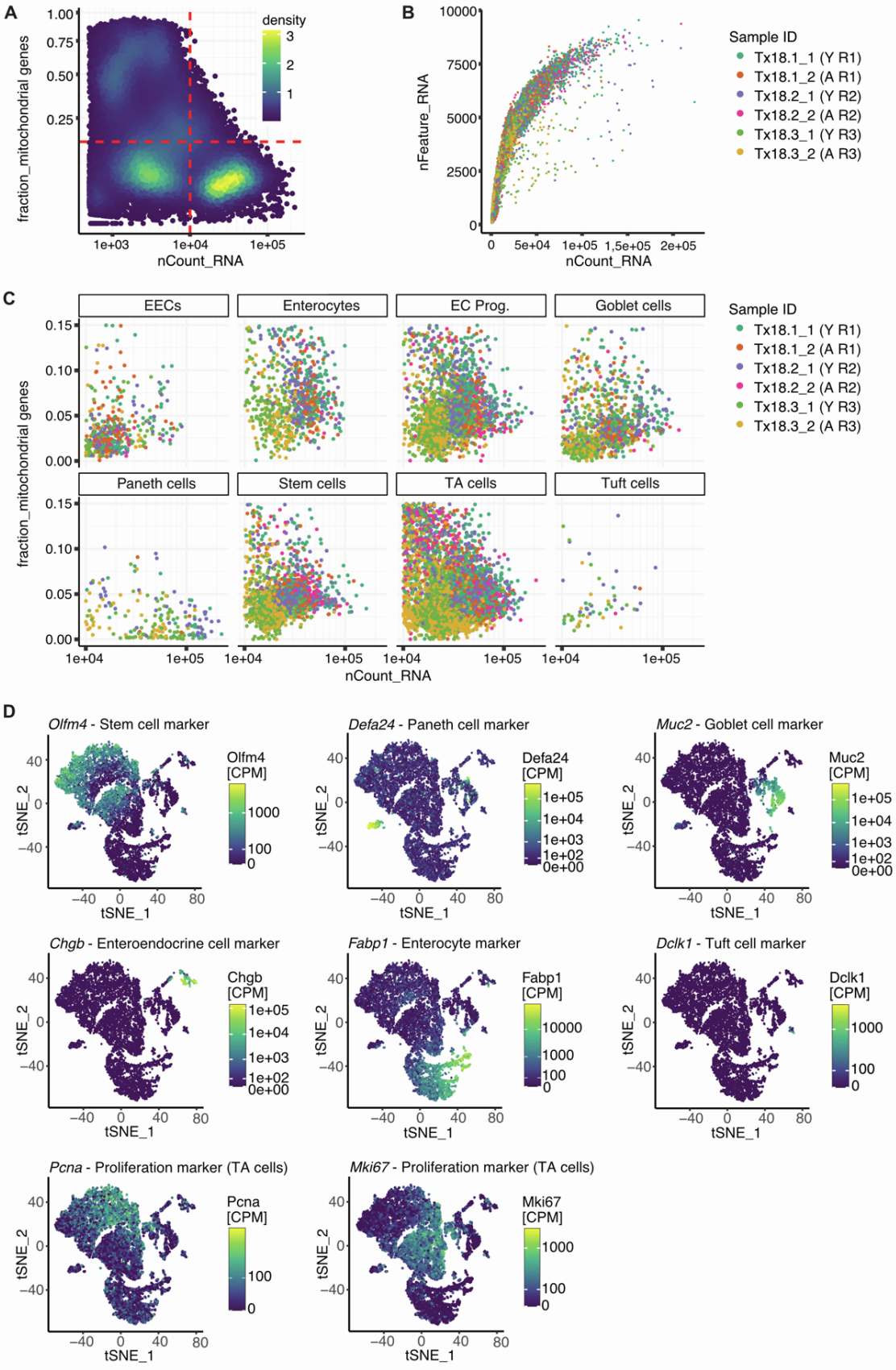
A
fraction_mitochondrial genes
nCount_RNA
density
B
nFeature_RNA
nCount_RNA
Sample ID
Tx18.1_1 (Y R1)
Tx18.1_2 (A R1)
Tx18.2_1 (Y R2)
Tx18.2_2 (A R2)
Tx18.3_1 (Y R3)
Tx18.3_2 (A R3)
C
EECs
Enterocytes
EC Prog.
Goblet cells
Paneth cells
Stem cells
TA cells
Tuft cells
D
Olfm4 - Stem cell marker
Defa24 - Paneth cell marker
Muc2 - Goblet cell marker
Chgb - Enteroendocrine cell marker
Fabp1 - Enterocyte marker
Dclk1 - Tuft cell marker
Pcna - Proliferation marker (TA cells)
Mki67 - Proliferation marker (TA cells)
tSNE_1
tSNE_2

**Figure S2. QC *in vivo* single-cell RNA-Seq of the proximal small intestinal epithelium. Related to Figure 2.**

**(A)** Fraction of UMI counts from mitochondrial genes and total UMI counts of all droplets passing cellranger's filters. To restrict analysis to alive and intact cells, transcriptomes with more than 10 000 total counts (dotted red line) and less than 15 % of counts from mitochondrial genes (dashed red line) were selected.

**(B)** The number of genes observed over the total number of UMI counts for each cell. Shows the same typical saturating relationship for each sample (indicated by color) and thus, despite varying cell numbers and average UMI counts, no quality issues of individual samples.

**(C)** Quality control plot similar to (A) but subset to the selected, high-quality cells and split up by the assigned cell type and colored by sample. Reveals some dependency of QC measures on cell type (e.g. lower number of total counts for EECs and lower fraction of counts from mitochondrial genes for Paneth cells) but indicates no strong bias against certain cell types due to the QC filtering.

**(D)** tSNE visualization of all sequenced cells (13 360) and color-coded for expression of one representative cell type marker per cell type: Stem cell marker *Olfm4*, Paneth cell marker *Defa24*, Goblet cell marker *Muc2*, Enteroendocrine marker *Chgb*, Enterocyte marker *Fabp1*, Tuft cell marker *Dclk1* and Proliferation marker for transit-amplifying cells *Pcna* and *Mki67*. Color-scale is log(100 + . )-transformed.

EEC: enteroendocrine cells, EC Prog.: enterocyte progenitor, TA: transit-amplifying cells.

## Figure S3

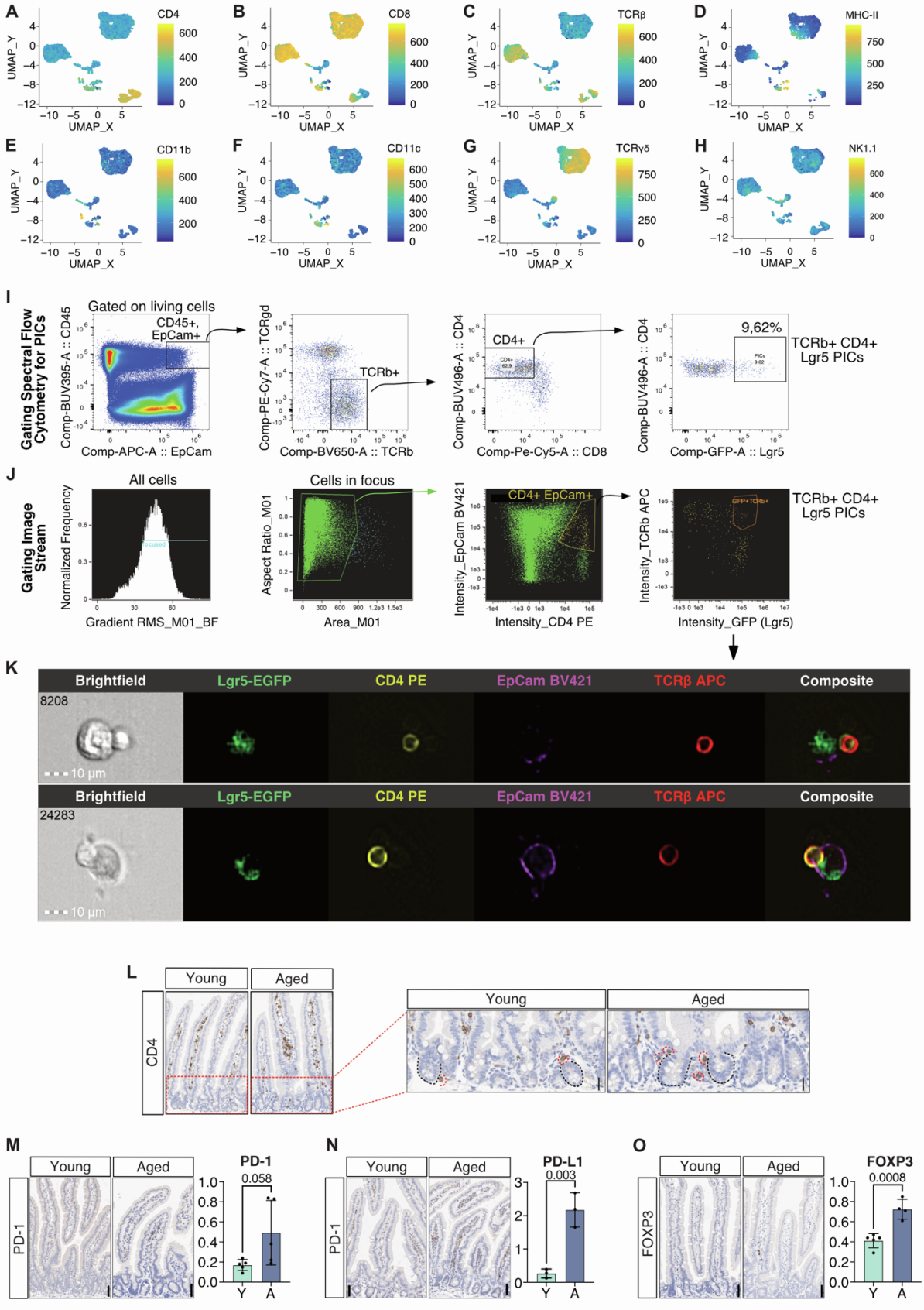
A
CD4
B
CD8
C
TCRβ
D
MHC-II
E
CD11b
F
CD11c
G
TCRγδ
H
NK1.1
UMAP_X
UMAP_Y
I
Gating Spectral Flow Cytometry for PICs
Gated on living cells
CD45+, EpCam+
TCRb+
CD4+
9,62%
TCRb+ CD4+ Lgr5 PICs
Comp-APC-A :: EpCam
Comp-BV650-A :: TCRb
Comp-Pe-Cy5-A :: CD8
Comp-GFP-A :: Lgr5
J
Gating Image Stream
All cells
Cells in focus
CD4+ EpCam+
TCRb+ CD4+ Lgr5 PICs
Gradient RMS_M01_BF
Area_M01
Intensity_CD4 PE
Intensity_GFP (Lgr5)
K
Brightfield
Lgr5-EGFP
CD4 PE
EpCam BV421
TCRβ APC
Composite
8208
24283
10 µm
L
Young
Aged
CD4
M
PD-1
0.058
N
PD-L1
0.003
O
FOXP3
0.0008
Y
A

**Figure S3. The immune microenvironment of the ageing intestine.**
**Related to Figure 4.**

**(A-H)** UMAP display of surface measurements of hematopoietic cell type markers on $CD45^+$ hematopoietic cells from young and aged mice as described in (4A). Colors indicate the expression level of the respective marker.

**(I)** Gating strategy to identify $CD45^+$ $EPCAM^+$ double positive cells and quantification of $Lgr5^+$ $CD4^+$ cells among these double positive cells.

**(J)** Gating strategy to image ISC-$CD4^+$ interaction pairs as Lgr5-EGFP, EpCam-BV421 and CD4-PE, $TCR\beta^+$-APC positive cells by image flow cytometry.

**(K)** Two examples of visualized ISC-$CD4^+$ interaction pairs by image flow cytometry based on the gating strategy shown in (J).

**(L)** IHC stainings against CD4 in the small intestine of young and aged mice. Left: Red boxes indicate zoom into the crypt region, as shown on the right. Right: Intestinal crypts are highlighted with black dashed lines, $CD4^+$ T cells with red dashed lines; scale bar = 50 μm.

**(M-O)** IHC staining and quantification as a percentage of respective positive cells for (M) PD-1, (N) PD-L1, and (O) FOXP3 in whole intestinal tissue sections from young and aged mice. Displayed images show representative stainings per age. Bars represent the average percentage for all young (n=3-5) and all aged mice (n=3-4) ± SD and data points represent the percentage for the individual biological replicate; statistical significance was tested by an unpaired t-test (two-sided), and p-Value is indicated on the respective comparison; scale bar = 50 μm.

UMAP: Uniform Manifold Approximation and Projection, ISC: Intestinal stem cell, IHC: Immunohistochemistry.

## Figure S4

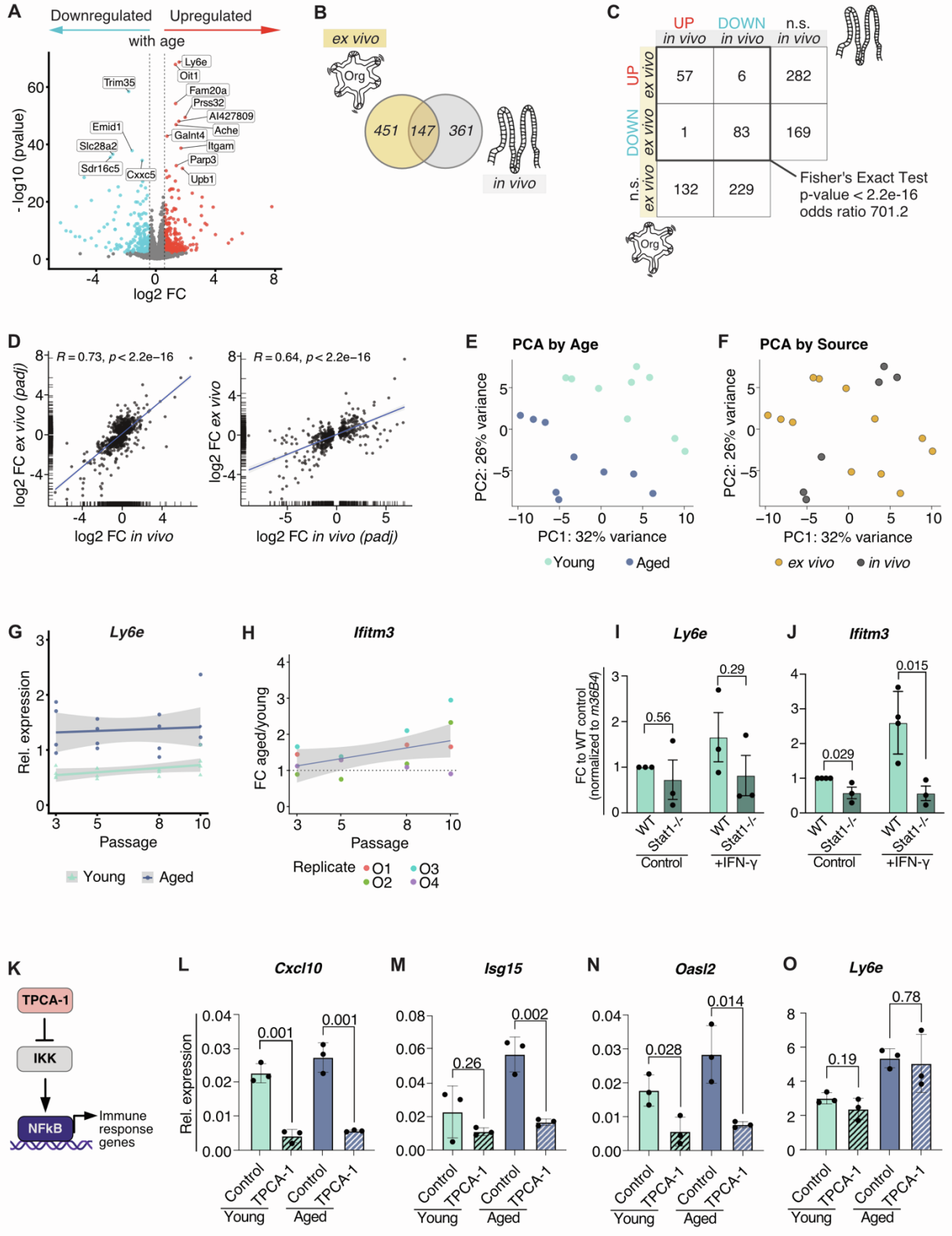
A
Downregulated
Upregulated
with age
- log10 (pvalue)
log2 FC
Ly6e
Oit1
Trim35
Fam20a
Prss32
AI427809
Emid1
Ache
Galnt4
Slc28a2
Itgam
Parp3
Sdr16c5
Cxxc5
Upb1
B
ex vivo
Org
451
147
361
in vivo
C
UP in vivo
DOWN in vivo
n.s. in vivo
UP ex vivo
DOWN ex vivo
n.s. ex vivo
57
6
282
1
83
169
132
229
Org
Fisher's Exact Test
p-value < 2.2e-16
odds ratio 701.2
D
R = 0.73, p < 2.2e−16
log2 FC ex vivo (padj)
log2 FC in vivo
R = 0.64, p < 2.2e−16
log2 FC ex vivo
log2 FC in vivo (padj)
E
PCA by Age
PC2: 26% variance
PC1: 32% variance
Young
Aged
F
PCA by Source
PC2: 26% variance
PC1: 32% variance
ex vivo
in vivo
G
Ly6e
Rel. expression
Passage
Young
Aged
H
Ifitm3
FC aged/young
Passage
Replicate O1 O2 O3 O4
I
Ly6e
FC to WT control (normalized to m36B4)
0.56
0.29
WT
Stat1-/-
Control
+IFN-γ
J
Ifitm3
0.029
0.015
WT
Stat1-/-
Control
+IFN-γ
K
TPCA-1
IKK
NFkB
Immune response genes
L
Cxcl10
Rel. expression
0.001
0.001
Control
TPCA-1
Young
Aged
M
Isg15
0.26
0.002
N
Oasl2
0.028
0.014
O
Ly6e
0.19
0.78

**Figure S4. *Ex vivo* bulk RNA-Seq from young and aged organoids.**
**Related to Figure 5.**

**(A)** Volcano plot showing DEGs upon ageing (aged over young) in small intestinal organoids, red: significantly (FDR≤10%) upregulated (log2FC > 0.5), blue: significantly downregulated (log2FC < 0.5), grey: not significant (FDR>10%, absolute log2FC < 0.5); gene names of the 15 most significantly changed genes upon ageing are plotted.

**(B)** VENN diagram showing the overlap of 147 significantly (FDR≤10%) DEGs (absolute log2FC > 0.5) upon ageing as determined by bulk RNA-seq, between *ex vivo* cultured intestinal organoids and *in vivo* intestinal epithelium.

**(C)** Matrix showing the numerical distribution of significantly (FDR≤10%) upregulated and downregulated genes upon ageing between *ex vivo* cultured intestinal organoids and *in vivo* intestinal epithelium. All gene names of DEGs are listed in Table S2. Fisher's Exact test was applied to assess the significance of the association between genes upregulated or downregulated *in vivo* and *ex vivo* in the same direction versus random, p-value < 2.2e-16.

**(D)** Correlation of the effects of ageing on the transcriptome as determined by bulk RNA-seq in intestinal organoids (y-axis) and *in vivo* intestinal epithelium (x-axis). A Deming regression line, as well as the Pearson correlation coefficient R and a p-value (p) of a test for correlation, are shown. Left correlation plot: only genes significantly (FDR≤10%) affected in intestinal organoids (*ex vivo*) are included. Right correlation plot: only genes significantly (FDR≤10%) affected in freshly isolated intestinal epithelial cells (*in vivo*) are included.

**(E-F)** Intestinal organoids display a stable age effect in a joint analysis of bulk RNA-Seq data of young and aged *ex vivo* cultured intestinal organoids and *in vivo* intestinal epithelium. Color indicates in (E) the age of the samples, in (F) the source of the samples.

**(G)** Transcript levels of *Ly6e* over the time course of 10 passages (11 weeks of culture) in young and aged small intestinal organoids by qRT-PCR (normalized to *36B4*) (n=4 different organoid lines per age), data points representing the result of each biological replicate.

**(H)** Fold change (aged over young) expression of *Ifitm3* in intestinal organoids over the time course of 10 passages (11 weeks of culture). Transcript levels were assessed in young and aged small intestinal organoids by qPCR (normalized to *36B4*) (n=4 per age).

**(I-J)** Transcriptional changes of (I) *Ly6e* and (J) *Ifitm3* in wildtype (WT) and Stat1 knockout (Stat1-/-) organoids in control and IFNγ (500pg/ml, 6hrs) treatment conditions. Transcript levels were assessed by qRT-PCR (normalised to *36B4*) in n=3 biological replicates per age and treatment and calculated as fold change compared to WT control condition. Data are represented as mean ± SD and data points represent the result of each biological replicate. Statistical significance was tested by an unpaired t-test (two-sided); p-values are indicated on respective comparisons.

**(K)** Schematic of TPCA-1 as IKK inhibitor, blocking NF$\kappa$B signaling.

**(L-O)** Transcriptional changes of (L) *Cxcl10,* (M) *Isg15*, (N) *Oasl2* and (O) *Ly6e* in young and aged organoids in control and TPCA-1 (5μM, 24 hrs) treatment conditions. Transcript levels were assessed by qRT-PCR (normalised to *36B4*) in n=3 biological replicates per age and treatment. Data are represented as mean ± SD and data points represent the result of each biological replicate. Statistical significance was tested by an unpaired t-test (two-sided); p-values are indicated on respective comparisons.

DEGs: differentially expressed genes, log2FC: log2 fold change.

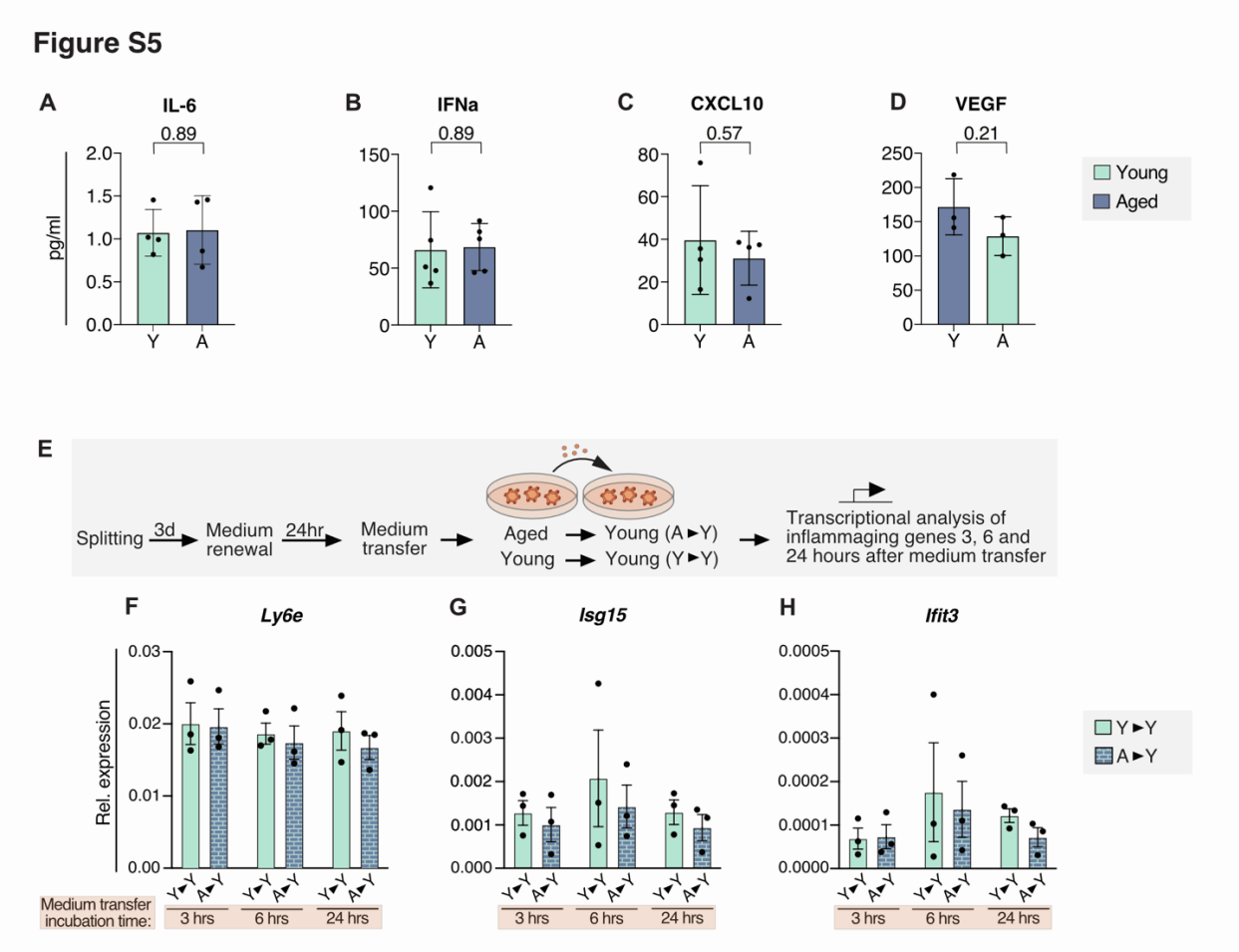


**Figure S5. Secreted factors are not the major source of intrinsic inflammaging in aged intestinal organoids.**

**Related to Figure 5 and 6.**

**(A-D)** Electrochemiluminescence-based cytokine assay to measure SASP-associated cytokines (A) IL-6, (B) IFNα, (C) CXCL10, (D) VEGF. Data are represented as mean ± SD and data points represent the result of each biological replicate. Statistical significance was tested by an unpaired t-test (two-sided), p-Value is indicated on respective comparison.

**(E)** Schematic of functional secretome assay.

**(F-H)** Transcriptional changes of (F) *Ly6e*, (G) *Isg15*, and (H) *Ifit3* in young organoids exposed to secretome of young (Y>Y) or aged (A>Y) organoids for 3, 6, or 24 hours according to the experimental procedure outlined in (E). Transcript levels were assessed by qRT-PCR (normalised to *36B4*) in n=3 biological replicates per age and treatment. Data are represented as mean ± SEM and data points represent the result of each biological replicate.

# Figure S6

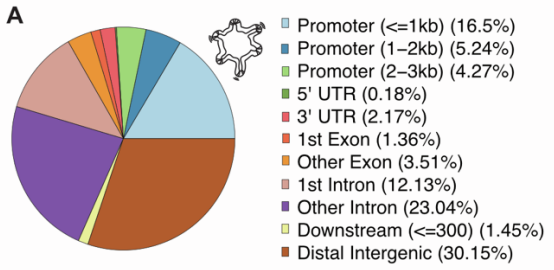
A
Promoter (<=1kb) (16.5%)
Promoter (1–2kb) (5.24%)
Promoter (2–3kb) (4.27%)
5' UTR (0.18%)
3' UTR (2.17%)
1st Exon (1.36%)
Other Exon (3.51%)
1st Intron (12.13%)
Other Intron (23.04%)
Downstream (<=300) (1.45%)
Distal Intergenic (30.15%)

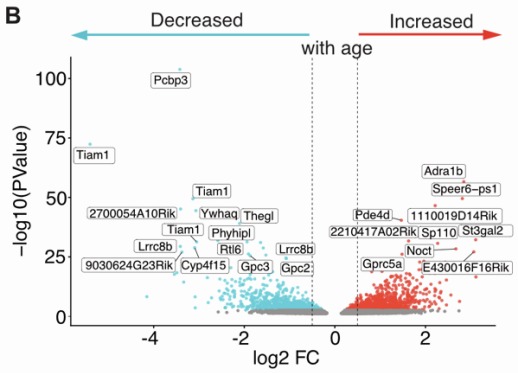
B
Decreased
Increased
with age
−log10(PValue)
log2 FC
Pcbp3
Tiam1
Adra1b
Speer6-ps1
2700054A10Rik
Ywhaq
Thegl
Pde4d
1110019D14Rik
Phyhipl
2210417A02Rik
Sp110
St3gal2
Lrrc8b
Rtl6
Noct
9030624G23Rik
Cyp4f15
Gpc3
Gpc2
Gprc5a
E430016F16Rik

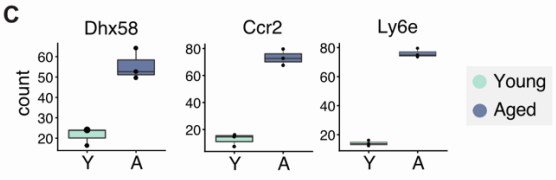
C
Dhx58
Ccr2
Ly6e
count
Young
Aged
Y
A

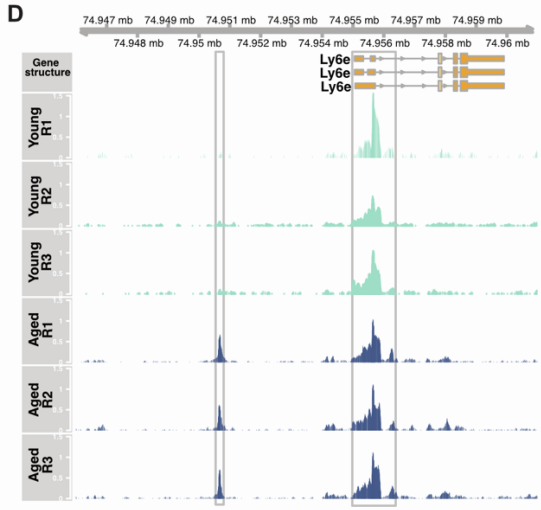
D
Gene structure
Ly6e
Young R1
Young R2
Young R3
Aged R1
Aged R2
Aged R3

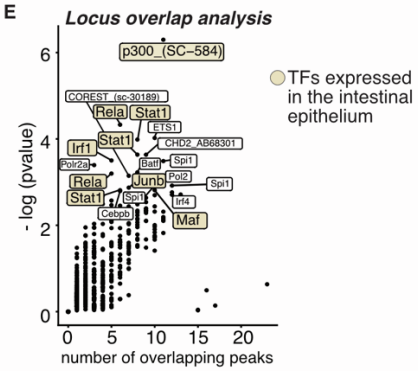
E
Locus overlap analysis
p300_(SC-584)
TFs expressed in the intestinal epithelium
- log (pvalue)
number of overlapping peaks

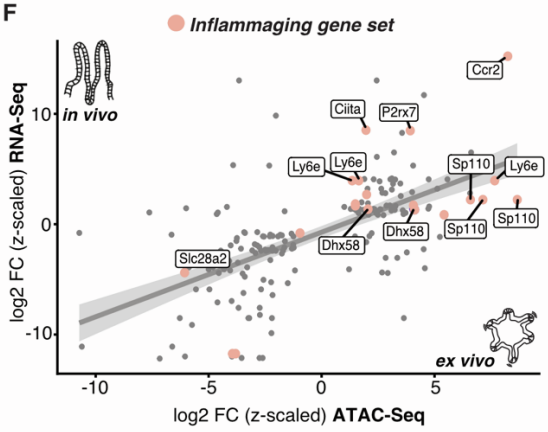
F
Inflammaging gene set
in vivo
ex vivo
log2 FC (z-scaled) RNA-Seq
log2 FC (z-scaled) ATAC-Seq
Ccr2
Ciita
P2rx7
Ly6e
Sp110
Dhx58
Slc28a2

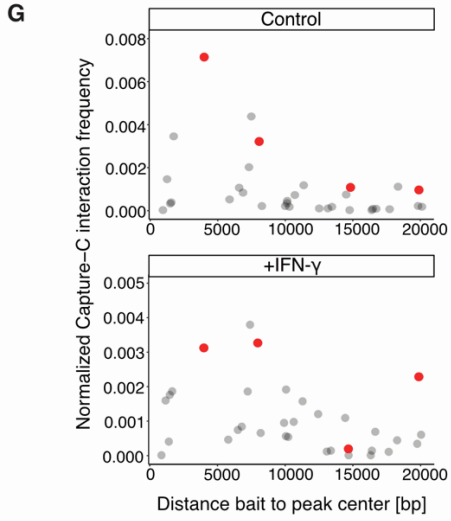
G
Control
+IFN-γ
Normalized Capture–C interaction frequency
Distance bait to peak center [bp]

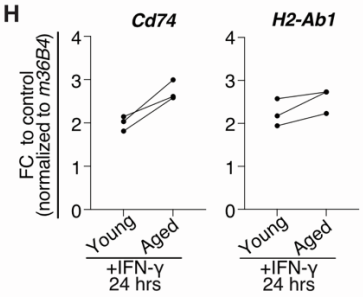
H
Cd74
H2-Ab1
FC to control (normalized to m36B4)
Young
Aged
+IFN-γ 24 hrs

**Figure S6. Chromatin remodelling accompanies inflammaging in the intestinal epithelium. Related to Figure 6.**

**(A)** Pie chart represents the distribution of mapped regions of the ATAC-Seq experiment from *ex vivo* intestinal organoids across genomic regions.

**(B)** Chromatin accessibility in intestinal epithelial cells undergoes changes upon ageing and is persistent during *ex vivo* culture. Volcano plot showing significantly (FDR≤10%) changed peaks of chromatin accessibility in genetic regions/loci upon ageing (aged over young) in small intestinal organoids derived from young (n=3) and aged (n=3) mice; 25 most significantly changed chromatin peaks are labeled, red: increased (log2FC > 0), blue: reduced (log2FC < 0), grey: not significantly changed (FDR>10%).

**(C)** Count plots for *Dhx58*, *Ccr2* and *Ly6e* for differentially open chromatin regions determined by ATAC-Seq. Bars represent the average counts for all young and all aged samples, dots represent the counts of the individual sample.

**(D)** Peak density in the regulatory region assigned to *Ly6e* as assessed in intestinal organoids is shown for all young (n=3) and aged (n=3) samples in genomic coordinates close to *Ly6e* by R/Gviz. Peaks of chromatin accessibility are color-coded by the age of the sample.

**(E)** Locus Overlap Analysis (LOLA) determines enriched overlap between annotated transcription factor (TF) bindings sites and open chromatin regions of the ATAC-Seq experiment in intestinal organoids. Color highlighted are TFs expressed in the intestinal epithelium based on our RNA-Seq data.

**(F)** Scatterplot of the effects of ageing on the expression of genes as determined by bulk RNA-seq of *in vivo* intestinal epithelium (y-axis, z-scaled log2 FC) and on the chromatin accessibility as determined by ATAC-Seq in intestinal organoids (x-axis, z-scaled log2 FC). Genes of the inflammaging gene set are color-highlighted and a linear regression line indicates the agreement between the compared data sets (95 % CI shaded grey). Only genes significantly (FDR≤10%) affected *in vivo* intestinal epithelium are included.

**(G)** Normalized Capture-C interaction frequencies between ATAC-peaks and gene promoters, plotted by the distance of peak center to promoter-overlapping bait center for control (top) and IFNγ-treated (bottom) organoids. Only promoters with total coverage within 20% of *Ciita*_TSS1 are shown. Red dots represent interactions of the induced ATAC-peak highlighted in Figures 6D-E with *Ciita* TSS_1-3 (as annotated in Figure 6D).

**(H)** Transcriptional changes of (G) *Cd74* and (H) *H2-Ab1* in young and aged organoids in control or IFNγ (2ng/ml) treatment conditions. Transcript levels were assessed by qRT-PCR (normalised to *36B4*) in n=3 biological replicates per age and treatment. Fold changes upon IFNγ treatment compared to control are plotted and data points from individual experiments are linked.

Log2FC: log2 fold change.

## Figure S7

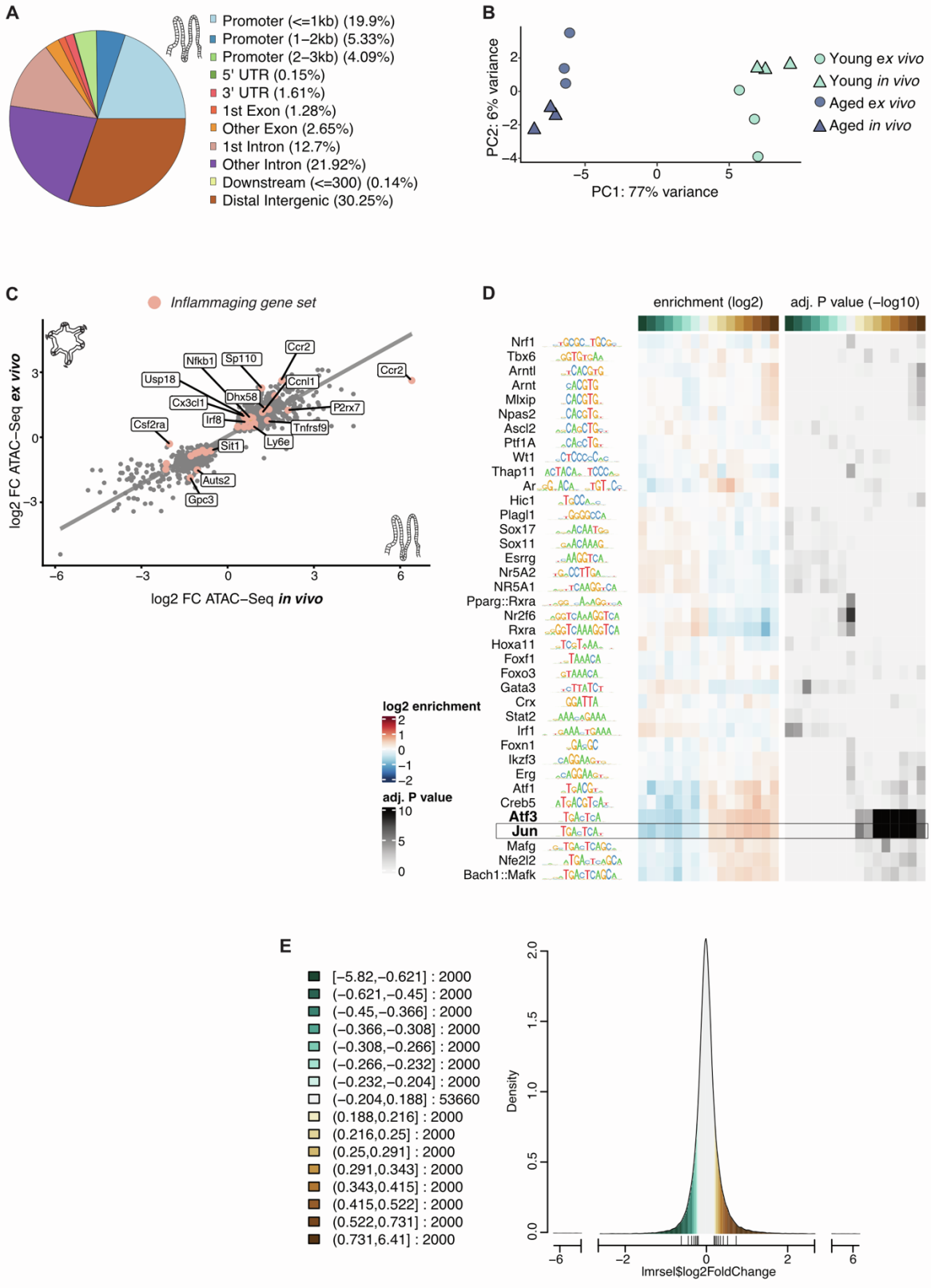
A
Promoter (<=1kb) (19.9%)
Promoter (1–2kb) (5.33%)
Promoter (2–3kb) (4.09%)
5' UTR (0.15%)
3' UTR (1.61%)
1st Exon (1.28%)
Other Exon (2.65%)
1st Intron (12.7%)
Other Intron (21.92%)
Downstream (<=300) (0.14%)
Distal Intergenic (30.25%)
B
PC2: 6% variance
PC1: 77% variance
Young ex vivo
Young in vivo
Aged ex vivo
Aged in vivo
C
Inflammaging gene set
log2 FC ATAC–Seq ex vivo
log2 FC ATAC–Seq in vivo
Ccr2
Nfkb1
Sp110
Usp18
Ccnl1
Dhx58
Cx3cl1
P2rx7
Irf8
Tnfrsf9
Csf2ra
Ly6e
Sit1
Auts2
Gpc3
D
enrichment (log2)
adj. P value (–log10)
log2 enrichment
adj. P value
Nrf1
Tbx6
Arntl
Arnt
Mlxip
Npas2
Ascl2
Ptf1A
Wt1
Thap11
Ar
Hic1
Plagl1
Sox17
Sox11
Esrrg
Nr5A2
NR5A1
Pparg::Rxra
Nr2f6
Rxra
Hoxa11
Foxf1
Foxo3
Gata3
Crx
Stat2
Irf1
Foxn1
Ikzf3
Erg
Atf1
Creb5
Atf3
Jun
Mafg
Nfe2l2
Bach1::Mafk
E
[–5.82,–0.621] : 2000
(–0.621,–0.45] : 2000
(–0.45,–0.366] : 2000
(–0.366,–0.308] : 2000
(–0.308,–0.266] : 2000
(–0.266,–0.232] : 2000
(–0.232,–0.204] : 2000
(–0.204,0.188] : 53660
(0.188,0.216] : 2000
(0.216,0.25] : 2000
(0.25,0.291] : 2000
(0.291,0.343] : 2000
(0.343,0.415] : 2000
(0.415,0.522] : 2000
(0.522,0.731] : 2000
(0.731,6.41] : 2000
Density
lmrsel$log2FoldChange

**Figure S7. Age-related changes in chromatin accessibility of intestinal epithelial cells *in vivo*.**

**Related to Figure 7.**

**(A)** Pie chart represents the distribution of mapped regions of the ATAC-Seq experiment from *in vivo* freshly isolated intestinal epithelium across genomic regions.

**(B)** Intestinal organoids display a stable age effect in a joint principal component analysis of ATAC-Seq data of young and aged *ex vivo* cultured intestinal organoids and *in vivo* intestinal epithelium. Shape indicates the source of the samples, and color indicates the age of the samples.

**(C)** Scatterplot of the effects of ageing on chromatin accessibility as determined by ATAC-Seq of intestinal organoids (y-axis, log2 FC) and *in vivo* intestinal epithelium (x-axis, log2 FC). Genes of the inflammaging gene set are color-highlighted. A linear regression line indicates the agreement between the compared data sets. Only genes significantly (FDR≤10%) affected are included.

**(D)** Heat map showing binned motif enrichment analysis based on changes in chromatin accessibility upon ageing in freshly isolated *in vivo* intestinal epithelium by monaLisa identifies an enrichment for the transcription factors Jun and Atf4 in genomic regions gaining chromatin accessibility upon ageing.

**(E)** Bin distribution for binned motif enrichment analysis shown in (D).

Log2FC: log2 fold change.

| **Table S3. Primer sequences for qRT-PCR and genotyping of Lgr5-EGFP-IRES-creERT2 & Stat1 KO mouse lines.** | | |
|---|---|---|
| **Gene** | **Sequence Fwd Primer** | **Sequence Rev Primer** |
| *36B4* | 5'-CCGATCTGCAGACACACACT-3' | 5'-ACCCTGAAGTGCTCGACATC-3' |
| *Ly6e* | 5'-GCGGGCTTTGGGAATGTCA-3' | 5'-CGCCACACCGAGATTGAGAT-3' |
| *Igtp* | 5'-ATGGTGGTATGGCTTGTGGA-3' | 5'-GGGAGGTCTTGGTGTTCTCA-3' |
| *Ciita* | 5'-AAAGAGGCAGCAACAAGAGC-3' | 5'-AAGTACCTCTGCCAGACCAC-3' |
| *Cd74* | 5'-ATGGATGGCGTGAACTGGAA-3' | 5'-GTGGGCTTCTTCTCCTCCAG-3' |
| *H2-Ab1* | 5'-CATCACTGTGGAGTGGAGG-3' | 5'-CTCGAGGTCCTTTCTGACTC-3' |
| *Ifitm3* | 5'-TCTTCATGAACTTCTGCTGCC-3' | 5'-CATCACCCACCATCTTCCGA-3' |
| *Oasl2* | 5'-ATTAAGGTGGTGAAGGGAGG-3' | 5'-CCTGCTCTTCGAAACTGGA-3' |
| *Cxcl10* | 5'-CCATCACTCCCCTTTACCCA-3' | 5'-GCTTGACCATCATCCTGCAG-3' |
| *Isg15* | 5'-ATGGAGGACAAGGAGCTGC-3' | 5'-TCCCAAAAGTCCTCCATACCC-3' |
| *Ifit3* | 5'-ATCATGAGTGAGGTCAACCG-3' | 5'-AAATGTTCGACCTGGTTGC-3' |
| *Usp18* | 5'-GAGAGGACCATGAAGAGGA-3' | 5'-TAAACCAACCAGACCATGAG-3' |
| | | |
| **Allele** | **Sequence Fwd Primer** | **Sequence Rev Primer** |
| *Lgr5-EGFP* Mutant Rev | | 5'-CTGAACTTGTGGCCGTTTAC-3' |
| *Lgr5-EGFP* Wild type Rev | | 5'-GTCTGGTCAGAATGCCCTTG-3' |
| *Lgr5-EGFP* Common Fwd | 5'-CTGCTCTCTGCTCCCAGTCT-3' | |
| *Stat1* Mutant Rev | | 5'-TGTGGTTTCCAAATGTGTCAG-3' |
| *Stat1* Common Fwd | 5'-TGCACATGAGTTTATTCCACCT-3' | |
| *Stat1* WT Rev | | 5'-GGCGAGAAGCTGAGCA-3' |

| Table S4. Sequences Capture-C probes. | |
|---|---|
| Capture-C probe names | Capture-C probe sequence |
| af3750 Ciita_TSS1_CC20_R | ATAGGGTAAGCTTTTGGAAAACCTGGGTGGCTGGGTGCTGCAAGCACAAAGCTTGTTTTCCACATTGATC |
| af3751 Ciita_TSS2_CC20_L | GATCAGAGCAGCCAACACTGGCATGTCTTGGTGACACGCTGTCATGAGGATGGGACTTGGGCATCGTGTG |
| af3753 Ciita_TSS2_CC20_R | ATCTGGCACCGTGAAGTAACCACTGTCATCCGAGGTCCCCAGTGTAATGTTGGTGAAAAAGGGTGGGATC |
| af3754 Ciita_TSS3_CC20_L | GATCTGCCTGTAGGGAGGGGTCCTCTGGAAAGACTCAGTCCAAGCAAACTTGGGTTGCATGTGGCAGCTT |
| af3755 Ciita_TSS3_CC20_R | GGAGACTGCATGCAGGCAGCACTCAGAAGCACGGGGCACAGCCACAGCCGCGGTAGGTGTCTCCAAGATC |
| af1165_Klf4_CC_1 | CCAAAGTCAACGAAGATTAAAAACTTTAGAAACAAAACCTCAAACCAAAACCCCCAGATTGCCCGAGATC |
| af1166_Klf4_CC_2 | GATCACTCCGGCCCAAAGGGTCTCGAGACTTGTCCACCTAAAATATAGTGGACTGAGTGCGCCCACCCCA |
| af1229_Sox2_CC_1 | GATCGGCTAAAATTACCCTCTCGGGTCCTGGGCAGGCAAGATTCTTGAACCCCTACCCCCGCCCCCAGCC |
| af1230_Sox2_CC_2 | TGTTTTTTCATCCCAATTGCACTTCGCCCGTCTCGAGCTCCGCTTCCCCCCAACTATTCTCCGCCAGATC |
| af1201_Klf2_CC_1 | GATCTCTCTACTTTGATGTTTTGTGGAAAGGACCTGTGGACAGTTGGGGCTGATGTTACAGACCAGTGTC |
| af1202_Klf2_CC_2 | TGGGACAGGAGGTGGGTGCAGGGACTGAGGACACGCGCGCTGAAGGGATGCCGTGCACCGGGTGCAGATC |
| af1169_Phc1_CC_1 | GATCGGGGAGCCCGGCGGAGCGCGAGAAGCAGGGAGATAACCAGACAGCATGCTCGGATGGAAGGACCAA |
| af1170_Phc1_CC_2 | CGTGAAAGGGGGGGAAAAAAAGAAGGTATTTTCTGCAGCTTCTGGGAATAGGGGCTCGAAAGAAAGGATC |
| af1171_Sall4_CC_1 | GATCGCCCTCCTCGGGGGGTCCCCCAGAGGTGCGCCCCTCCCCCAGGGGCCCCCAAGAGGGTAGTAGAGA |
| af1172_Sall4_CC_2 | ATCAATAATGCATTGCGATTTATCATGAGCTCTGACAGCTGATTGGCCTGGGTCCAAGACCTCAGAGATC |
| af1173_Stat3_CC_1 | GATCTCCACCTGAGTGGCAGTGGCTCTGGTGGCCCGAACGTCCCTAGCCTCCGGGAGCAGTCACAGGAGG |
| af1174_Stat3_CC_2 | CCGAGGGCCGCCTGGCCTCTCCTAGCCGACGCGGTCAGGCGACACCGAGCGGGGTTGTACCTCAGCGATC |
| af1163_Esrrb.2_CC_1 | GATCCAGACCCGGGCTGGCATGTTTTGCCAGTATTTGTTGTGTGACCTGGAGAAGGACAATTCTGCACAC |
| af1164_Esrrb.2_CC_2 | TCTGGCGCTCCGCGTCCCATCGCGCTTCGGTGGAACTCGGAGCGTTCGTTGTGCGGTCCTGGAAATGATC |
| af1167_Nanog_CC_1 | GATCAGAGGATGCCCCCTAAGCTTTCCCTCCCTCCCAGTCTGGGTCACCTTACAGCTTCTTTTGCATTAC |
| af1168_Nanog_CC_2 | GGCTGCGGCTCACTTCCTTCTGACTTCTTGATAATTTTGCATTAGACATTTAACTCTTCTTTCTATGATC |
| af2328_Lifr_CC_1 | GATCCGTTTCTTCTCTGCACAAATAAGCCCAACACGCCTCAGAGGCACGACTAGATGGCTCCAGGATGTT |
| af2329_Lifr_CC_2 | AGGCAAGCAAAGTTAGGCTTCCTAATGGATGGCTTTCCGGATGTGTTGTCTAAAGCACAAAGCTGAGATC |
| af2330_Tfcp2l1_CC_1 | GATCGGGGTCCGAGCGCTGACTAACCTCAGGCCTCCAGAGAAGGGCCCTCCGGGAGGCCCCTAGGGAATG |
| af2331_Tfcp2l1_CC_2 | TTTTTCTTTTAAAAAATAACTCCAAACCATTGAAAATGGTAATCAAACTAGGGACATGAGACTGCAGATC |
| af2332_Dppa5a_CC_1 | GATCAAGCTTATCCACCACGCACGGCCCACAGCTCCAGGTTCAGGAAGTTTTAGTACCTGTGTGGGCGGT |
| af2333_Dppa5a_CC_2 | CGCTGGAAAGTTCAAAGACTTCTAAAAGACTATAGCTTTTCCCATCCCGAAAGAATCAGATACTGGGATC |